International Journal of Nanomedicine

Dovepress
open access to scientific and medical research

Open Access Full Text Article

ORIGINAL RESEARCH

Synthesis, Characterization, Biomedical Application, Molecular Dynamic Simulation and Molecular Docking of Schiff Base Complex of Cu(II) Supported on Fe_3O_4/SiO_2/APTS

This article was published in the following Dove Press journal:
International Journal of Nanomedicine

Rahime Eshaghi Malekshah[1]
Bahareh Fahimirad[1]
Ali Khaleghian[2]

[1]Department of Chemistry, College of Science, Semnan University, Semnan, Iran; [2]Biochemistry Department, Faculty of Medicine, Semnan University of Medical Sciences, Semnan, Iran

Introduction: Over the past several years, nano-based therapeutics were an effective cancer drug candidate in order to overcome the persistence of deadliest diseases and prevalence of multiple drug resistance (MDR).

Methods: The main objective of our program was to design organosilane-modified Fe_3O_4/SiO_2/APTS(~NH_2) core magnetic nanocomposites with functionalized copper-Schiff base complex through the use of (3-aminopropyl)triethoxysilane linker as chemotherapeutics to cancer cells. The nanoparticles were characterized by Fourier transform infrared spectroscopy (FT-IR), X-ray powder diffraction (XRD), field emission scanning electron microscopy (FE-SEM), TEM, and vibrating sample magnetometer (VSM) techniques. All analyses corroborated the successful synthesis of the nanoparticles. In the second step, all compounds of magnetic nanoparticles were validated as antitumor drugs through the conventional MTT assay against K562 (myelogenous leukemia cancer) and apoptosis study by Annexin V/PI and AO/EB. The molecular dynamic simulations of nanoparticles were further carried out; afterwards, the optimization was performed using MM+, semi-empirical (AM1) and Ab Initio (STO-3G), ForciteGemo Opt, Forcite Dynamics, Forcite Energy and CASTEP in Materials studio 2017.

Results: The results showed that the anti-cancer activity was barely reduced after modifying the surface of the Fe_3O_4/SiO_2/APTS nanoparticles with 2-hydroxy-3-methoxybenzaldehyde as Schiff base and then Cu(II) complex. The apoptosis study by Annexin V/PI and AO/EB stained cell nuclei was performed that apoptosis percentage of the nanoparticles increased upon increasing the thickness of Fe_3O_4 shell on the magnetite core. The docking studies of the synthesized compounds were conducted towards the DNA and Topoisomerase II via AutoDock 1.5.6 (The Scripps Research Institute, La Jolla, CA, USA).

Conclusion: Results of biology activities and computational modeling demonstrate that nanoparticles were targeted drug delivery system in cancer treatment.

Keywords: superparamagnetic, Schiff base, core–shell, MTT assay, apoptosis, molecular docking, computational methods, Topoisomerase II

Correspondence: Ali Khaleghian
Department of Biochemistry, Faculty of Medicine, Semnan University of Medical Sciences, 5th Km Damghan Road, P.O. Box 3514533, Semnan 3513138111, Iran
Fax +98 2333654202
Email khaleghian.ali@gmail.com

Introduction

Owing to their unique physical properties, small size, biocompatibility, and low toxicity, nano superparamagnetic iron oxide nanoparticles (SPION) have attracted scientific interest in the areas of biotechnology and biomedicine.[1–3] Nanotherapeutics, a new platform of nano-medicine development, is utilized in the rapidly growing

cancer and cellular therapies.[4–6] Nanostructured materials functionalized with organic or inorganic coatings were developed as alternatives for the clinical studies of cancer therapy through attacking solid tumors.[6–11] The use of magnetic nanoparticles was introduced as a novel technical approach for cancer diagnosis and treatment with optimum anti-cancer effects.[12] Furthermore, L-lysine, L-arginine and 3-aminopropyltriethoxysilane (APTES) were employed to coat negatively charged nanoparticles; this increased the chances of nanoparticles binding to the anionic cell membrane. Iron oxide nanoparticles coated with these compounds prevented the oxidation of nanoparticles.[13] To treat tumors, the poor penetration and effectiveness of anticancer drugs can be overcome through improving magnetic-targeted carrier designs.[14] Ag/Fe_3O_4NPs can be utilized as a promising alternative for water purification and antibacterial properties.[15,16] Gupta et al reported the synthesis of core–shell magnetic nanostructures coated with (3-aminopropyl)triethoxysilane (APTES) linked with PEG diacid for magnetic resonance imaging (MRI). The results showed that these nanoparticles Fe_3O_4 could potentially be used for MR imaging in cancer diagnosis.[3] Azadbakht et al showed that 3-aminopropyltriethoxy silane (APTES)-polyethylene glycol (PEG) coated iron oxide nanoparticles had therapeutic effects and targeting efficacy in terms of cancer therapy.[17] Nigam et al showed that nanoparticles (Glu–Fe_3O_4) with polyethylene glycol polyamidoamine exhibited anticancer activity against HeLa cell strains.[18] Fe_3O_4 core functionalized with APTES as carriers for MR was synthesized and tested for targeted morin drug delivery by Saif. The results showed that up to 60% of the adsorbed drug was released within 4 h.[19] In another research, magnetic nanoparticles of cathelicid in ll-37 peptide were synthesized and assessed regarding the proliferation of colon cancer cells (HT-29 cells).[20] In addition, to increase the solubility and bioavailability of magnetic iron oxide nanoparticles (MIONs), Rifampicin (RIF) cross-linked Polyethylene glycol hybrid Chitosan (mCSPEG) gel beads were utilized.[21] The properties of poly(D,L-lactide-co-glycolic acid) (PLGA) based magnetic microspheres (MMS) as a curcumin delivery carrier against HeLa cell lines were further investigated. The magnetic microspheres exhibited good properties as anti-cancer drugs.[22] Copper ions are essential for cellular processes such as respiration, neural transmission, dopamine-b-hydroxylase, superoxide dismutase, cytochrome c oxidase, tissue maturation, defense against oxidative stress and iron metabolism, ascorbate in ascorbate oxidase and catechols in tyrosinase or laccases, and cofactors for a number of enzymes.[23,24] Copper ion deficiency can lead to Wilson's disease, Parkinson's disease, and Menkes syndrome.[25,26] Accordingly, in the present work, Fe_3O_4/SiO_2/APTS(~NH_2) was primarily synthesized and then functionalized by Schiff base complex Cu(II). Finally, the anticancer activity of each synthesized nanoparticle was assessed and compared for the first time. Moreover, the optimized structures were investigated by quantum chemical theory calculations and molecular dynamics simulations; these structures were then employed to explore the internal relationship between the inhibitory efficiency of compounds and the molecular structure of receptors (DNA and Topoisomerase II).

Methods

Chemicals and Instruments

All chemical reagents and solvents at the highest purity were purchased from Merck and Sigma–Aldrich Chemical Companies, including: $FeCl_2.4H_2O$, $FeCl_3.6H_2O$, HCl (37%), NH_4OH, tetraethyl ortho silicate (TEOS), 3-aminopropyl triethoxysilane (APTS), 2-hydroxy-3-methoxybenzaldehyde, $Cu(OAc)_2.2H_2O$, toluene, methanol, and acetonitrile, being of the highest available purity, were supplied from the Merck Company. Cell lines were obtained from National Cell Bank of Iran [NCBI]-Pasteur Institute of Iran. The Dulbecco's modified eagle medium-high glucose (DMEM), fetal bovine serum (FBS) and penicillin-streptomycin were obtained from Gibco BRL (Life Technologies, Paisley, Scotland). The culture plates were obtained from Nunc (Roskilde, Denmark). MTT [3-(4,5′-dimethyltiazol-2-yl)-2,5-diphenyltetrazolium bromide] was purchased from Sigma. Chem. Co. (Munich, Germany). FT-IR spectra of complexes were used in KBr pellets on a SHIMADZU UV-1650PC. The XRD data were collected on a Bruker D8000 Germany in a scanning range of 2θ = 10–90° and CuK_α radiation. To observe the particle morphology, field emission scanning electron microscopy (FE-SEM) and Transmission Electron Microscopy (TEM) on HITACHI S-4160 and Jeol, JEM-1010, respectively, were recorded. VSM of nanoparticles was registered on a vibrating sample magnetometer (VSM) MDKFD.

Synthesis of Compounds

Preparation of the Magnetic Fe_3O_4 and Fe_3O_4/SiO_2 Nanoparticles

To synthesize Fe_3O_4 nanoparticles, 6 g of $FeCl_3.6H_2O$ and 2 g of $FeCl_2.4H_2O$ were primarily dissolved in 100 mL deionized water and sonicated for 20 min. Afterwards,

10 mL of ammoniac solution was added to it under a nitrogen atmosphere at 80°C. After 1 h, the black sediment was cooled and collected by an external magnetic field. Finally, Fe_3O_4 nanoparticles were washed with distilled water and dried at 60°C overnight. Next, 1 g of Fe_3O_4 nanoparticles was dispersed in 100 mL of ethanol/H_2O. Therefore, 1.5 mL of ammoniac solution was added dropwise and sonicated for 30 min. In the next step, 10.5 mL TEOS was added and stirred for 16 h. The sediment (Fe_3O_4/SiO_2) was separated and washed with a mixture of water and methanol.[27]

Preparation of Fe_3O_4/SiO_2/APTS Core Shell

To synthesis of Fe_3O_4/SiO_2/APTS, 1 g of Fe_3O_4/SiO_2 was dispersed in 25 mL toluene by ultrasonic and then 2 mL of (3-aminopropyl) triethoxysilane (APTS (~NH_2)) was added and refluxed at 110°C for 12 h. The resulting sediment was separated, washed and finally dried at 50 °C overnight.[27]

Preparation of Fe_3O_4/APTS(~NH_2)-Schiff Base Nanoparticles

To a solution of 0.4 mg of Fe_3O_4/SiO_2/APTS(~NH_2) in 20 mL methanol, 0.22 mg of 2-hydroxy-3-methoxybenzaldehyde in methanol (25 mL) was added dropwise. The mixture was refluxed at 60°C for 24 h. After completion of the reaction, the nanoparticles were separated by an external magnet and washed with methanol to remove no reacted species. Then, black magnetite solid product dried at 80°C under vacuum.

Synthesis of Fe_3O_4/SiO_2/APTS(~NH_2)-Schiff Base/Cu(II) Nanoparticles

To solution of the Fe_3O_4/SiO_2/APTS(~NH_2)-Schiff base nano-magnetic (0.2 g, 20 mL MeOH) was added $Cu(OAc)_2.2H_2O$ (0.2 g) in methanol. Then, the resultant mixture was refluxed at 60°C for 48 h. The resulting product was separated by an external magnet and washed with acetone and deionized water, then dried in vacuum at 80°C for 6 h.

Biological Studies

Preparation of Cell Culture

The cell lines K562 (a human erythroleukemia cancer) were cultured in Minimum Essential Medium of Iscove's Modified Dulbecco's Medium (IMDM) with inactivated 10% fetal bovine serum (Sigma), 104 U/mL penicillin-streptomycin as antibiotics (Biosera, Ringmer, East Sussex, UK) in plates and incubated in 2% CO_2 incubator at 37°C with 5% CO_2 (Heraeus, Hanau, Germany). The cells should have 80–90% confluence before the experiments.

Assessment of Cytotoxicity Using MTT Assay

To evaluate cytotoxicity effect of Fe_3O_4, Fe_3O_4/SiO_2/APTS (~NH_2), Fe_3O_4/SiO_2/APTS(~NH_2)-Schiff base and Fe_3O_4/SiO_2/APTS(~NH_2)-Schiff base-Cu(II), these compounds were determined using MTT colorimetric assay at K562 (myelogenous leukemia cancer) cells. The K562 cells at the density of 1×10^3 per well were cultured into 96 well tissue culture plates and allowed to grow. After the required incubation period and washing with PBS buffer (pH 7.4), different concentrations of nanoparticles 1–1000 µg/mL were added to the wells and maintained in a humidified atmosphere 5% CO_2 for 48 h. To examine the cell viability, after treatments of the nanoparticles, 20 µL of MTT (5 mg/mL) to form insoluble purple formazan crystals was added to each well for an additional 4 h. Then, the medium of the plate was removed and 100 µL of dimethyl sulfoxide was added to each well to dissolve the MTT formazan crystals. The assay was performed in triplicate and the cytotoxic effect was expressed as percentage of cell viability relative to untreated control cells. Finally, the plates including the amount of formazan crystal formation were agitated at high speed and the absorbance of samples was measured by measuring at 570 nm.

Acridine Orange/Ethidium Bromide Doubles Staining (AO/EB) Assay

The cell lines K562 were seeded in 48-well plates (10^4 cells per well) and incubated for 24 h. The medium was removed and replaced with another medium containing the Fe_3O_4/SiO_2/APTS, Fe_3O_4/SiO_2/APTS~Schiff base and Fe_3O_4/SiO_2/APTS~ Schiff base-Cu(II) with 1–1000 µg/mL for 48 h. The medium of compounds was again removed, the cells were washed with phosphate buffer saline (PBS), and fixed with trypsin before count and fluocytorimetric analyses. Cells were centrifuged for 5 mins and stained with AO/EB solution (AO: EB, 100 mg/mL) for 10–15 mins. Furthermore, the cells immediately were viewed using an inverted fluorescence microscope (Moticam Pro 252B).

Computational Methods

The compounds (as flexible ligand) (Fe_3O_4/SiO_2/APTS, Fe_3O_4/SiO_2/APTS~Schiff base; Fe_3O_4/SiO_2/APTS~Schiff base-Cu(II)) were optimized using DMol3 and Castep in Materials studio 2017. The energy (eV), space group, lattice parameters (Aº) and unit cell parameters (Aº) of the

predicted structures were taken from the CASTEP module of Materials Studio for the charge distributions.

Molecular Docking of the Compounds with DNA Duplex of Sequenced (ACCGACGTCGGT)2 (PDB ID: 1BNA) and Ribonucleotide Reductase (PDB ID: 3hne1)

Molecular docking simulation was performed to better fathom the antitumor activity and binding site of the target-ligand. The crystal structures of 1BNA (B-DNA Dodecamer: right-handed double-stranded B helix (as rigid molecule) with the sequence (5′-D(CpGpCpGpApApTpTpCpGpCpG)-3′) (as rigid molecule)), anti-cancer chemotherapeutic drugs (Mitoxantrone and Trifluridine (FTD) as DNA-drug interaction), Topoisomerase II (PDB ID: 4fm9), and Doxorubicin (as Topoisomerase II inhibitors) were downloaded from RCSB Protein Data Bank (ww.rcsb.org/pdb) and Pubchem. The compounds (as flexible ligand) were optimized using DMol3 and Castep in Materials studio 2017 and used as PDB format. The molecular docking simulation and calculations were performed by AutoDock1.5.6 (The Scripps Research Institute, La Jolla, CA, USA) with AutoGrid 4 and AutoDock 4 to predict the binding affinity and hydrogen bond interactions between the compounds and receptor. First of all, water molecules and other heteroatoms around the duplex were removed using the AutoDock tools; next, polar hydrogen atoms, Kollman united atom type charges, and Gasteiger partial charges were added to the receptor molecule as a target. All the docking simulations were defined by use of a grid box along the x-, y-, and z-axes (98 × 126 × 126 Å points) with a grid-point spacing of 0.375 Å for BNA; a grid box along the x-, y-, and z-axes (126 × 126× 126 Å) was further used with a grid-point spacing of 0.908 Å for Top II. To study this interaction, we employed the molecular docking using a Lamarckian Genetic Algorithm (LGA) method. The number of genetic algorithm runs and the number of evaluations were set to 100. The most optimal model with the lowest energy was picked up from the one minimum energy (root mean square deviation, RMSD = 0.0) from the 100 runs to compare the structural similarity. The interactions of BNA and Interleukin and their binding modes with compounds were then analyzed using an

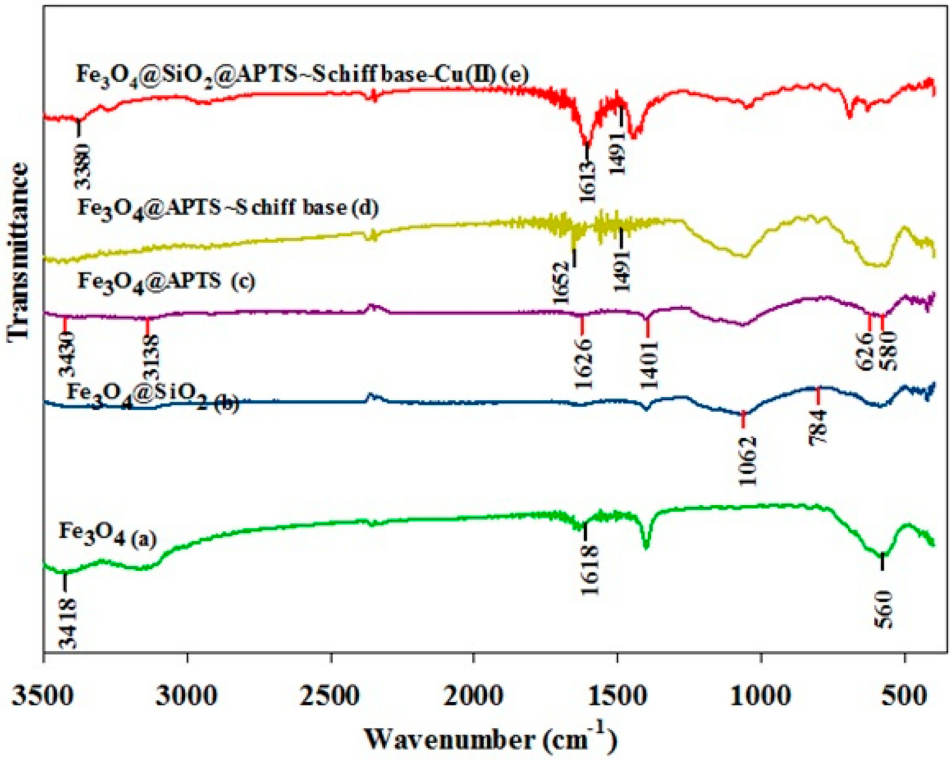

Figure 1 FTIR spectra of (**a**) bare Fe_3O_4 MNPs; (**b**) Fe_3O_4/SiO_2; (**c**) Fe_3O_4 MNPs treated by APTES; (**d**) Fe_3O_4 MNPs coated by Schiff base; (**e**) Fe_3O_4/SiO_2/APTS~Schiff base-Cu(II).

AutoDock program, UCSF Chimera 1.5.1 software, Discovery Studio 3.0 from Accelrys and DS Visualizer.

Results and Discussion

Infrared Spectra of Complexes

Figure 1a–e, respectively, shows the FT-IR analysis for Fe_3O_4, Fe_3O_4/SiO_2, Fe_3O_4/SiO_2/APTS(~NH_2), Fe_3O_4/SiO_2 /APTS(~NH_2)-Schiff base, and Fe_3O_4/SiO_2/APTS(~NH_2)-Schiff base-Cu(II) nanoparticles. In Figure 1a, the peak at 560 cm^{-1} shows the stretching vibration of Fe-O, confirming the presence of the magnetite nanoparticles of Fe_3O_4.[28] A broad and strong band and the other band appearing at 3418 and 1618 cm^{-1} are associated with the vibration of O-H stretching. Figure 1b shows the peak at 1062 and 718 cm^{-1}, indicating the Si-O-Si stretching vibration related to SiO_2 shells. In addition, Figure 1c shows the peak at 1401 cm^{-1}, which is related to the C=C stretching vibration. Stretching vibrations were further observed at 626 and 580 cm^{-1}, corresponding to the split of the v_1 of the Fe–O bond band at 560 cm^{-1} (Figure 1c).[29] The bands at 3430 and 1626 cm^{-1} of Figure (c) were attributed to the N–H stretching vibration and NH_2 bending mode of the coupling agent APTES, respectively.[29,30] Furthermore, the presence of vibration band at 3138 cm^{-1} showed the existence of hydrogen-bonded silanols in Fe_3O_4/SiO_2/APTS (Figure 1c).[31] The stretching vibration of C=N of the Schiff base was observed at around 1652 cm^{-1}; moreover, the υ(C=N) absorption of the Schiff base shifted towards the lower frequency in complex (1613 cm^{-1}), suggesting the coordination through azomethine nitrogen.[32,33] The stretching vibrations at 3380, 2870–3100, 1480–1600, and 1491 cm^{-1} were attributed to O-H stretching, CH stretching, C=C aromatic ring stretching, and CH_2 bending, respectively (Figure 1e).

XRD Spectra

Figure 2a and b, respectively, shows the crystal structures of Fe_3O_4/SiO_2 and Fe_3O_4/SiO_2/APTS(~NH_2)~Schiff base-Cu(II) nanoparticles. In these figures, the peaks at 2Θ = 30.1°, 34.7°, 42.3°, 56.2°, 57.1°, and 62.5° by indices of (2 2 0), (3 1 1), (4 0 0), (4 2 2), (5 1 1), and (4 4 0), in accordance with JCPDS3 standard No. 19–0629, are related to the Fe_3O_4 nanostructures.[34] Also, in Figure 2a, the broad peak below 30° indicates the existence of SiO_2 amorphous structures. The increased peak width in Figure 2b 30° implies the existence of organic structures on the surface of Fe_3O_4/SiO_2, corroborating the formation of the Fe_3O_4/SiO_2 /APTS(~NH_2)~Schiff base-Cu(II) structure.

VSM

Figure 3 shows the magnetic property of the synthesized samples studied through analyzing the vibrating sample magnetometer (VSM). According to Figure 3a, the maximum saturation magnetization for Fe_3O_4/SiO_2 components was 61.6 $emug^{-1}$; however, the maximum saturation magnetization for Fe_3O_4/SiO_2/APTS(~NH_2)-Schiff base-Cu(II) nanoparticles was 30.80 (Figure 3b). The difference in the

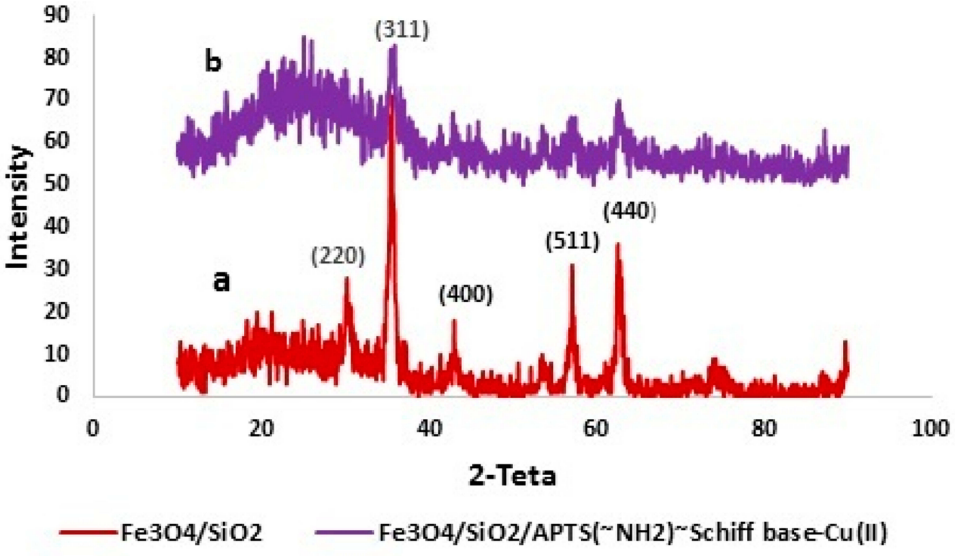

Figure 2 XRD patterns of Fe_3O_4/SiO_2 (**a**) and Fe_3O_4/SiO_2/APTS~Schiff base-Cu(II) (**b**).

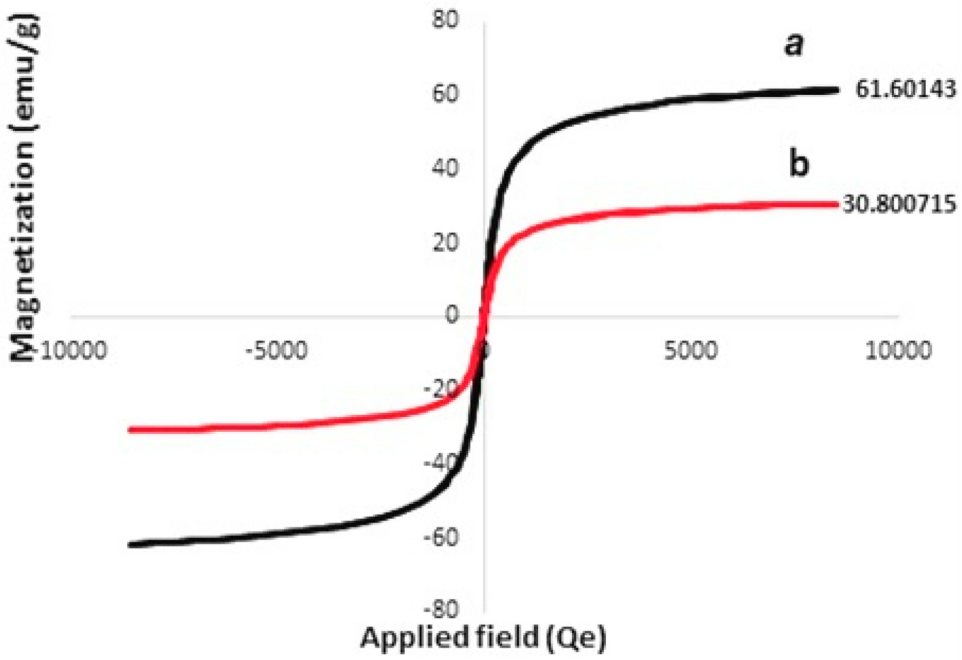

Figure 3 VSE of Fe_3O_4/SiO_2 (**a**) and Fe_3O_4/SiO_2/APTS~Schiff base-Cu(II) (**b**).

maximum saturation magnetization can well prove the presence of APTS~Schiff base-Cu(II) nanoparticles on the Fe_3O_4/SiO_2 surface. However, even with the reduction in the maximum saturation magnetization of Fe_3O_4/SiO_2 /APTS(~NH_2)~Schiff base-Cu(II) nanoparticles, they are still highly magnetic and can be easily collected from the solution with the help of an applied magnetic field.

FE-SEM

Figure 4 shows the surface morphology of the nanomaterials of Fe_3O_4 and Fe_3O_4/SiO_2/APTS(~NH_2)-Schiff base-Cu(II) nanoparticles. Figure 4A shows the thoroughly distributed spherical particles of Fe_3O_4. Based on this figure, the particle sizes of Fe_3O_4 nanoparticles were about 10 nm. Figure 4B and C show Fe_3O_4/SiO_2 /APTS-Schiff base-Cu(II) nanoparticles with different magnifications (200 and 500 nm). Figures a, b and c show that after modifying Fe_3O_4 surface by SiO_2, APTS, and Schiff base-Cu(II), no changes occurred in the surface morphology of Fe_3O_4. Moreover, the uniform sizes of Fe_3O_4/SiO_2/APTS~Schiff base-Cu(II) nanoparticles reached about 20 nm, which is a suitable

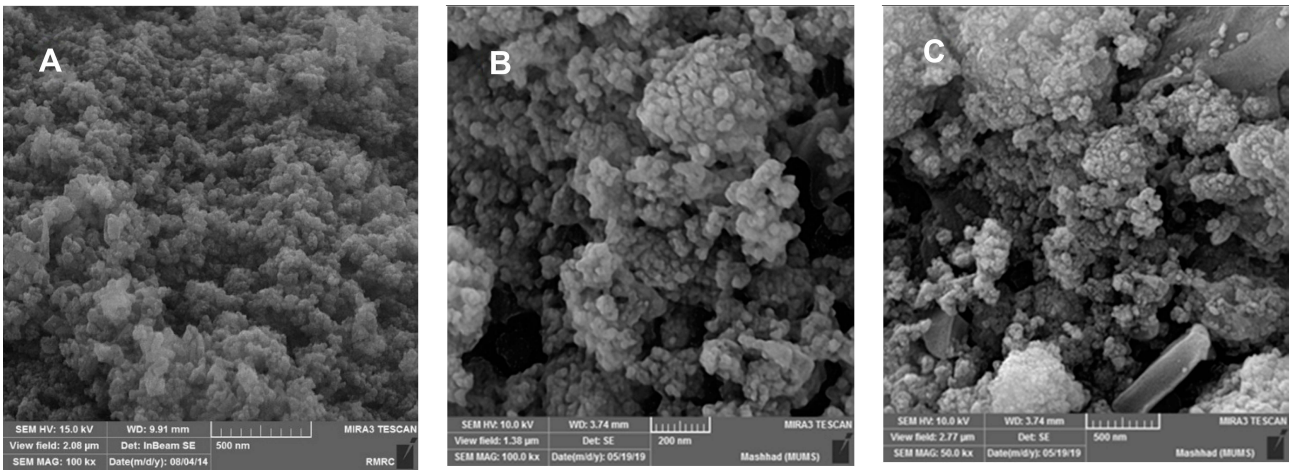

Figure 4 FE-SEM images of Fe_3O_4 (**a**); Fe_3O_4-APTS (**b**); Fe_3O_4/SiO_2/APTS~Schiff base-Cu(II) nanoparticles (**c**).

size for biomedical applications.[33] The increase in the particle size of Fe_3O_4/SiO_2/APTS~Schiff base-Cu(II) in comparison with Fe_3O_4 confirms the presence of a SiO_2 /APTS~Schiff base-Cu(II) on the Fe_3O_4 surface.

TEM

The size and morphology of the nanoparticles were determined by Transmission electron microscopy (TEM). Accordingly, TEM analysis was performed to specify the particle size, particle agglomeration, and the structure of core-shell obtained from Fe_3O_4/SiO_2/APTS~Schiff base-Cu(II). Figure 5 shows the nanoparticles of Fe_3O_4/SiO_2 /APTS~Schiff base-Cu(II) at different magnifications. According to this figure, the nanoparticles had a spherical morphology, the particles were well dispersed, and agglomeration did not occur. Figure 5 further shows that the average particle size was about 15 cm, corresponding to the analysis results of SEM. In this figure, the dark regions are the core of the nanoparticles (Fe_3O_4), and the lighter regions represent the shell structure of nanoparticles (SiO_2/APTS~Schiff base-Cu (II)).

Biological Essays

Assessment of Cytotoxicity Using MTT Assay

Several cytotoxic studies have demonstrated the enhanced understanding of Iron Oxide Nanoparticles (IONPs) toxicity owing to its very low toxic effect on human body. Various physicochemical factors such as size, shape, charge, surface area, aggregation and coating Iron Oxide Nanoparticles (IONPs) play a major roles in toxicity investigations.

A significant difference was observed between the toxicity responses regarding the shape of IONPs. The rod-shaped IONPs (Fe_3O_4) significantly more necrosis in mouse macrophage cells compared with spherical IONPs. The accumulation in cytoplasm and aggregation in vacuoles were assigned to the rod-shaped IONPs and spherical IONPs, respectively.[35,36] Moreover, the (geno) toxicity findings of IONPs proved that ROS production (reactive oxygen species) was a major reason for apoptosis, inflammation, and cell death.[37,38] ROS such as anions, hydroxyl radicals, and hydrogen peroxide had significantly increased H_2O_2 production due to the higher ratios of Fe^{2+} and Fe^{3+} occurring in mitochondria. The release of ferric ions from nanoparticles in the lysosomes of kupffer cells and macrophages by hydrolysing enzymes played a key role in the NPs toxicity mechanism and induced the cell death of certain cancer cells through apoptosis.[39] IONPs can be degraded in the acidic lysosomes (pH~4.5) and release iron ions in the form of ferrous ions (Fe^{+2}) able to react with hydrogen peroxide through crossing mitochondrial membrane in the Fenton reaction to generate highly reactive hydroxyl radicals and ferric ions (Fe^{3+}). ROS (hydroxyl radicals) can directly damage DNA, proteins, polysaccharides, lipids and ATP-generating mitochondria (Figure 6).[40–42] Without coating the ferrite nanoparticles, they are rapidly cleared by macrophages due to the large surface area/volume ratios. The hydroxyl groups at the surface of iron oxide nanoparticles can directly bind to silanes (Fe-O-Si bonds) with opposite end functional groups (amines, thiols) able to interact with organic or inorganic molecules, hence their potential applications in biology and medicine. In this study, MTT assay was used to test the in vitro cytotoxicity of nanoparticles against K562 cell lines (a human erythroleukemia cancer) screened by various concentrations for

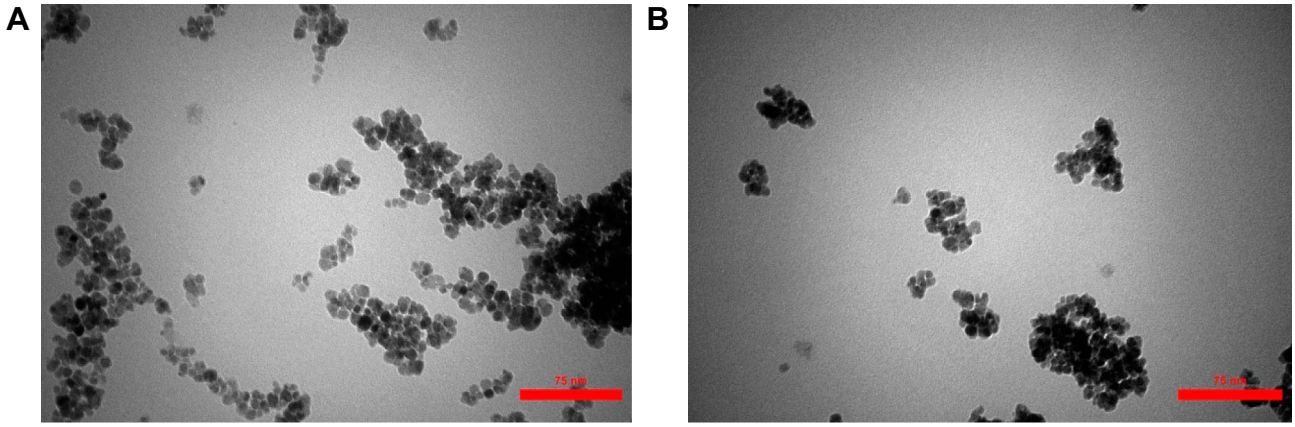

Figure 5 TEM images (**a**) and (**b**) of Fe_3O_4/SiO_2/APTS~Schiff base-Cu(II) nanoparticles at different magnifications.

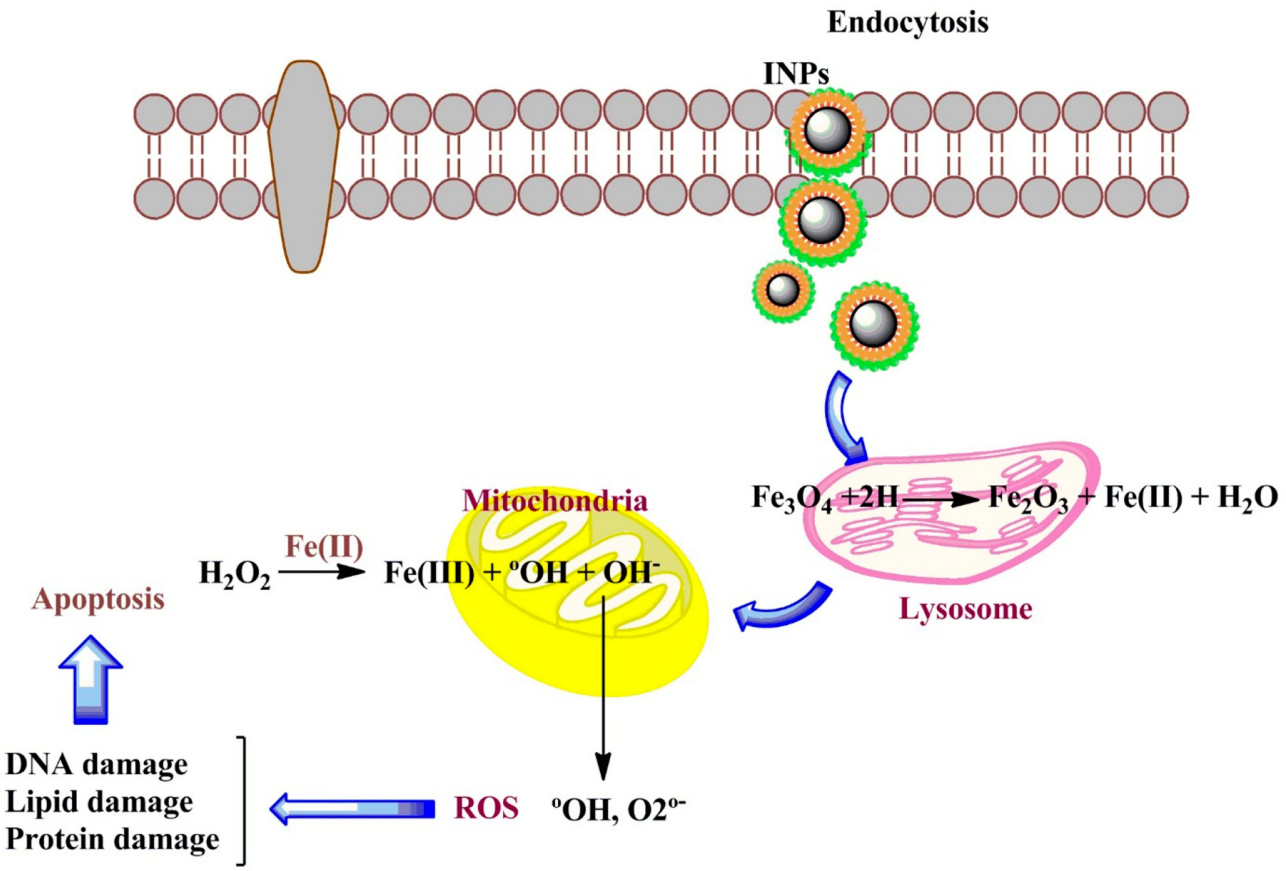

Figure 6 Schematic representation of intracellular uptake pathways and targets of INPs.

48 h. Figure 7 shows that the cytotoxic activities of nanoparticles augmented with the increase in the concentration of complexes. According to our results, the cell proliferation was obviously inhibited by all nano-compounds in a thick-dependent core-shell manner Fe_3O_4/SiO_2 /APTS(~NH_2) >Fe_3O_4/SiO_2/APTS(~NH_2)~Schiff base> Fe_3O_4/SiO_2/APTS(~NH_2)~Schiff base-Cu(II). The anticancer behavior of IONPs can be attributed to the charge

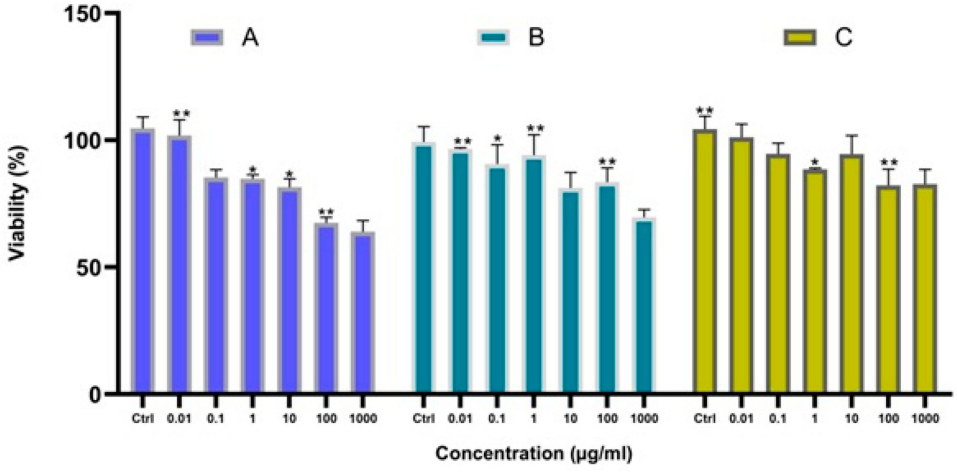

Figure 7 The anti-growth effect after the treatment with varying doses of Fe_3O_4/SiO_2/APTS (**a**); Fe_3O_4/SiO_2/APTS~Schiff base (**b**); Fe_3O_4/SiO_2/APTS~ Schiff base-Cu(II) (**c**) on K562 cell lines (myelogenous leukemia cancer) by the MTT as described in the experimental section. Data were normalized as a percentage of values of the control (*p<0.05 and **p<0.01).

on the surface of the resulting particles, which plays a major role in the intracellular uptake. The type of functional groups adds another complication to the in vitro test results. Positively charged IONPs such as amine-modified IONPs generate more ROS and toxicity compared to neutral and negatively charged IONPs. Researchers claim that the increased toxicity of nanoparticles can be ascribed to the strong electrostatic interaction between the positively charged spherical macro-ions and negatively charged membrane surfaces at higher doses. In fact, Amine-modified IONPs have exhibited higher lethal levels in in vitro tests owing to their strong interaction with negatively charged cell surface.[43,44] Therefore, NPs were functionalized with two different groups of APTES and Fe_3O_4 /SiO_2/APTS(~NH_2)~Schiff base with the aminosilane coating (positive surface charge) and Fe_3O_4/SiO_2 /APTS(~NH_2)~Schiff base coating (negative surface charge).[43,44] After coating, the high particle size of IONPs blocks the vessels and capillaries and inhibits embolization; therefore, it should remain in the submicron range.[45] The smaller IONPs can explain the higher toxicity compared to larger IONPs.[46] Therefore, in this study, NPs were functionalized with APTES, indicating the high cytotoxic activity against the K562 cell lines (a human erythroleukemia cancer).

Apoptosis Assay by AO/EB Stained Cell Nuclei

To compare the necrosis or early and late apoptosis effects on non-cancerous and cancer cell lines, the cells were subjected to treatment of compounds followed by Acridine orange/ethidium bromide double staining (AO/EB). Acridine orange dye stains both viable and nonviable cells owing to membrane permeability attaches to double-stranded nucleic acid (DNA), and emits green fluorescence. However, ethidium bromide dye stains nonviable, intercalates the DNA, emits red fluorescence, and destroys nuclear membrane integrity. A mixture of both dyes is commonly used to visualize nuclear membrane disintegration and apoptotic body formation that are characteristics of apoptosis. Three kinds of cells were observed according to the fluorescence emission and the morphological aspect of chromatin condensation: (i) normal cells appearing in organized structures with an intact nuclei stained with green fluorescence, (ii) early apoptotic cells, visible with bright green and light orange green colored fluorescence, and (iii) late apoptotic and necrotic nonviable cells with damaged cell membrane, condensed chromatin with orange to red green colored fluorescence.[47]

Cells were treated with 0.01, 0.1, 1, 10, 100 and 1000 μg/mL of each compound at 48 h (Figure 8). These morphological changes with concentrations 0.01, 0.1 and 1 μg/mL of Fe_3O_4/SiO_2/APTS, Fe_3O_4/SiO_2/APTS~Schiff base and Fe_3O_4/SiO_2/APTS~Schiff base-Cu(II) revealed that did not show any necrotic or apoptosis against the K-562 cancer cells. The concentrations 10, 100, 1000 μg/mL of Fe_3O_4/SiO_2/APTS showed Early/Late apoptotic and necrotic cells which were visible with bright green and light orange and red patches, respectively. Meanwhile, after treatment with Fe_3O_4/SiO_2/APTS~Schiff base nanoparticles at concentrates 100 and 1000 μg/mL, cells exhibit red colour, indicating late apoptotic with damaged cell membranes. In addition to, comparing at concentrate 1000 μg/mL of Fe_3O_4/SiO_2/APTS~Schiff base-Cu(II) revealed red colour that was related to late apoptotic. A comparison between these three compounds reveal that Fe_3O_4/SiO_2 /APTS and Fe_3O_4/SiO_2/APTS~Schiff base caused less apoptosis compared to uncoated INPs and inhibited the DNA replication through intercalation. Also, from Figure 8, it can be indicated that the apoptotic of nanoparticles increased with increasing concentration of nanoparticles and caused decreasing in live cells.

Annexin V/PI Dual Staining Assay

Increased research on the mechanisms of cell death over the past years has led to more understanding in terms of apoptosis and necrosis pathways. Double staining of Annexin V and propidium iodide stain was employed to analyze the early apoptotic, late apoptotic/necrotic, and dead cells via flow cytometry analysis. Apoptosis is the natural or programmed death of the cell by enzymes and necrosis is the uncontrolled and unprogrammed death, both occurring during cell death in response to cytotoxic conditions. Not programmed, necrosis is caused by an inflammatory reaction, toxins, trauma, infection and tissue damage due to the uncontrolled external factors in the external environment of the cell. During apoptosis, as a caspase-dependent pathway, fragmentation of nucleus, chromatin condensation, and blebbing of the plasma membrane are observed without integrity loss. Apoptosis, as an energy-dependent mechanism, and the exogenous pathway, the binding of FASL/TRAIL ligand and/or TNF-α (tumor necrosis factor α), bind to FASL/TRAIL receptor and TNFR1 receptors, respectively. This is able to transform procaspase-8 to caspase-8 through autohydrolysis. In

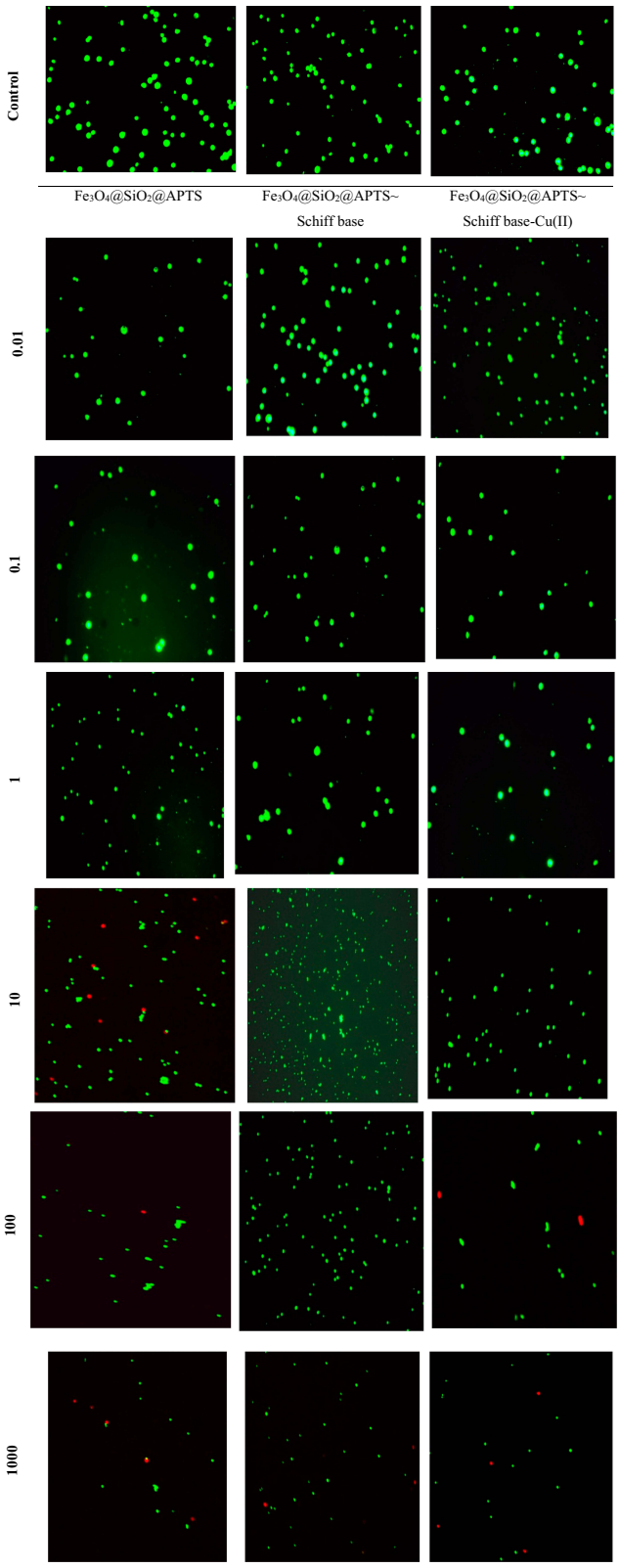

Figure 8 Acridine orange/ethidium bromide double staining for apoptosis analysis in cell lines K562 with treatment of 0.01, 0.1, 1, 10, 100 and 1000 μg/mL. Notes: Living cells, green fluorescence; apoptotic, orange fluorescence and necrotic cells and late apoptotic, red fluorescence.

type I cells, activated caspase-8 can activate caspase-3 and initiate apoptosis, thereby inducing cell death. In type II cells, as intrinsic apoptosis pathway, activated caspase-8 is capable of hydrolyzing Bid to tBid; tBid ten interacts with Bax/Bak (located on mitochondria) which is regulated by the Bcl-2 family proteins. Mitochondria is permeable by pore formation in the outer mitochondrial membrane; maintaining the integrity of lysosomes, mitochondria releases cytochrome c from the intermembrane space/or apoptosis-inducing factor (AIF). In addition, the cytochrome c released into the cytoplasm can interact with Apaf-1 and caspase-9 to activate caspase-3 and induce apoptosis. In turn, activates effector caspases which execute the cell death process by cleaving a range of cytoplasmic. Lamins and nuclear lamin-associated membrane proteins, the scaffold proteins of the nuclear envelope, are cleaved by effector caspases during caspase-mediated apoptosis, resulting in nuclear shrinkage and fragmentation. Plasma membrane blebbing results from the caspase-mediated activation and gelsolin enzyme, an actin depolymerizing enzyme.[48,49]

Phosphatidyl-l-serine on the plasma membrane surface (PS) exposure is a caspase-dependent process. Early apoptosis occurs at the cell surface. Annexin V-FITC is, a phospholipid-binding and calcium-dependent protein for detecting apoptosis and necrosis which binds to phosphatidylserine (PS) of plasma membrane translocated from the inner face to the outer plasma membrane. PS exposure to the outer leaflet of the plasma membrane can be recognized by phagocytes as a signal for engulfment. During necrosis as a caspase-independent pathway, no structural changes take place in chromatin and membrane integrity is loosened. Viable cells with intact membranes do not interact with either Annexin V or PI while the membranes of the dead and damaged cells are permeable to PI. Also, the cells interact with Annexin V in early apoptosis while the cells are already dead in late apoptosis (end stage apoptosis and death) and interact with Annexin V and PI. As shown in Figure 9, treatment of K562 cells was tested with nanoparticles at 1000 µg/mL. The percentage of viable cells treated with Fe_3O_4/SiO_2/APTS, Fe_3O_4/SiO_2/APTS~Schiff base, and Fe_3O_4/SiO_2/APTS~Schiff base-Cu(II) ranged from 8.03 and 0.92 to 4.58%, respectively. The percentages of late apoptosis with Fe_3O_4/SiO_2/APTS, Fe_3O_4/SiO_2/APTS~Schiff base and Fe_3O_4/SiO_2/APTS~Schiff base-Cu(II) ranged from 31.1, 40.9, and 17.3 to 76.9.3%, respectively, while no early apoptosis was observed. Our results showed that the late

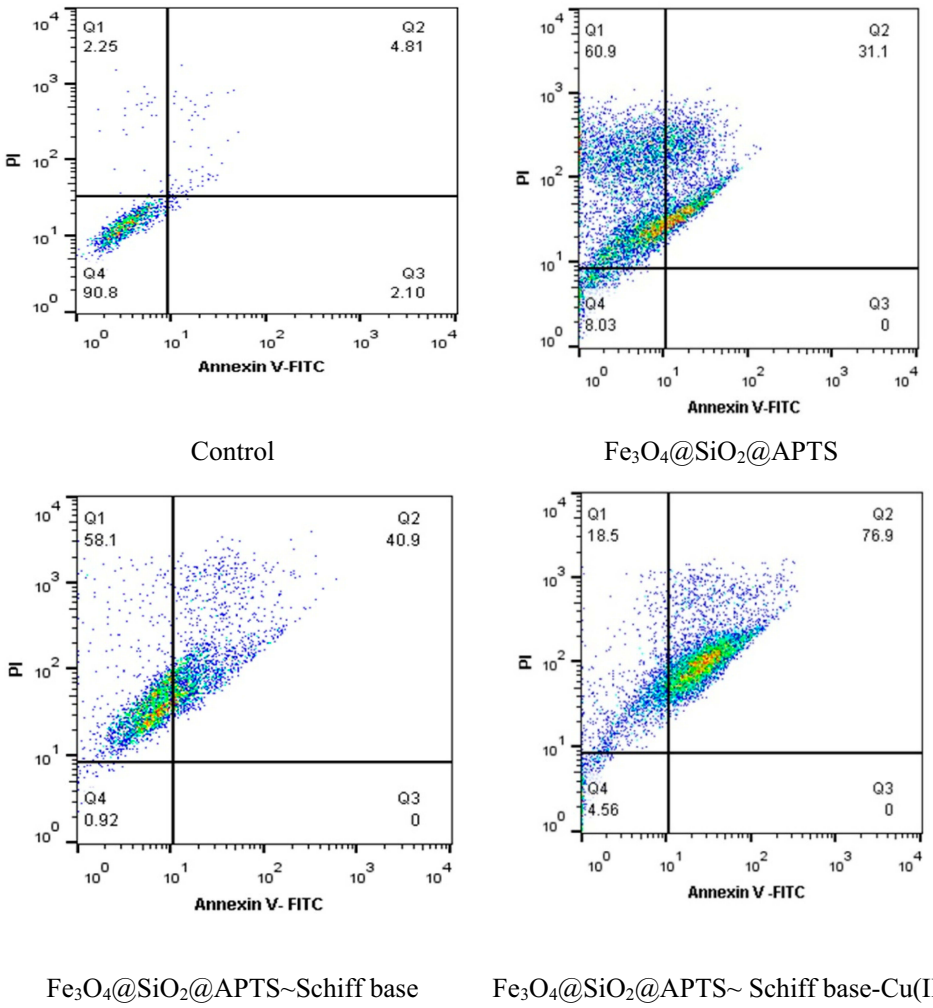

Figure 9 Flow cytometric analysis of nanoparticles against K562 by the FCM.

apoptosis percentage of the nanoparticles increased upon increasing the thickness of Fe_3O_4 shell on the magnetite core $Fe_3O_4/SiO_2/APTS$ < $Fe_3O_4/SiO_2/APTS$~Schiff base< $Fe_3O_4/SiO_2/APTS$~Schiff base-Cu(II). Therefore, $Fe_3O_4/SiO_2/APTS$~Schiff base-Cu(II) had more apoptosis compared with other compounds, suggesting a loss of plasma membrane integrity. In addition, the percentage of necrotic with $Fe_3O_4/SiO_2/APTS$, $Fe_3O_4/SiO_2/APTS$~Schiff base and Fe_3O_4/SiO_2

Table 1 CSP Results Showing List of Unique Crystal Structures[a] Ranked on the Basis of the Calculated Lattice Energy and Density

Compound	Fe_3O_4	$Fe_3O_4/SiO_2/APTS$	$Fe_3O_4/SiO_2/APTS$~Schiff Base	$Fe_3O_4/SiO_2/APTS$~Schiff Base-Cu(II)
Crystal system	Rhombohedral	Rhombohedral	Rhombohedral	Rhombohedral
Space group	*P*1	*P*1	*P*1	*P*1
a(Å)	6.034	8.466	9.953	9.721
b(Å)	6.034	8.466	9.953	9.721
c(Å)	6.034	8.466	9.953	9.721
α(°)	60.00	90.000	90.000	90.000
β(°)	60.00	90.000	90.000	90.000
γ(°)	60.00	90.000	90.000	90.000
Cell volume	–	606.957	986.055	918.772
Final energy	−8688.084 eV	−12,044.134 eV	−16,511.406 eV	−18,147.712 eV

Note: [a]Unit-cell geometrical parameters of compounds were determined in Materials studio 2017.

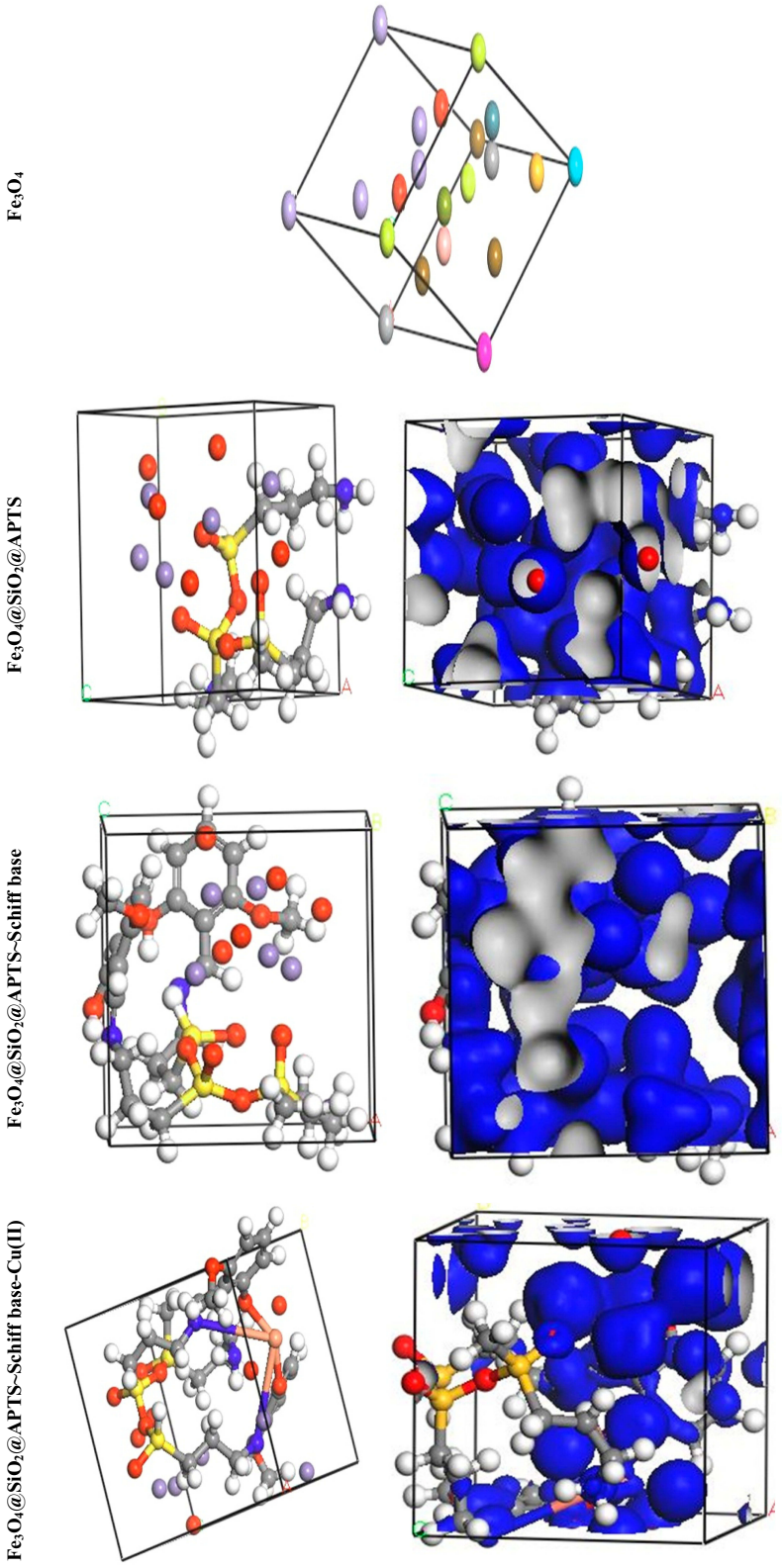

Figure 10 Perspective view and electron density of the optimized compounds Fe_3O_4, $Fe_3O_4/SiO_2/APTS$, $Fe_3O_4/SiO_2/APTS$~Schiff base and $Fe_3O_4/SiO_2/APTS$~Schiff base-Cu(II).

/APTS~Schiff base-Cu(II) ranged from 60.9 and 58.1 to 16.5% in K562 cells. Positively charged IONPs generated more percentages of necrotic compared to neutral and negatively charged IONPs.[50]

Simulation Methods

Crystal Structure Prediction (CSP) and Structural Analysis

The theoretical study was carried out by NVT (N, constant number of particles, V, constant volume, and T, constant temperature) and NPT (N, constant number of particles, P constant pressure, and T, constant temperature) 15 ns in the time and ensemble atomic simulation on compounds during molecular dynamics simulations. To further study the data collection and figures associated with the electron density of the optimized structures of Fe_3O_4, Fe_3O_4/SiO_2/APTS, Fe_3O_4/SiO_2/APTS~Schiff base, and Fe_3O_4/SiO_2/APTS~Schiff base-Cu(II), they are inserted in Table 1 and Figure 10. The Fe_3O_4, Fe_3O_4/SiO_2/APTS, Fe_3O_4/SiO_2/APTS~Schiff base, and Fe_3O_4/SiO_2/APTS~Schiff base-Cu(II) were crystallized in the Rhombohedralspace group *P*1. Crystal data of compounds are shown in Table 1. The results of molecular dynamics simulations showed that the cell volume of the compounds Fe_3O_4/SiO_2/APTS, Fe_3O_4/SiO_2/APTS~Schiff base, and Fe_3O_4/SiO_2/APTS~Schiff base-Cu(II) included 606.957, 986.055 and 918.772Å^3, respectively. Figures 10 and 11 show the calculated frontier orbital density distributions and intermolecular and π–π stacking interactions between the expand units of neighboring atoms in the supramolecular chains of Fe_3O_4/SiO_2/APTS, Fe_3O_4/SiO_2/APTS~Schiff base, and Fe_3O_4/SiO_2/APTS~Schiff base-Cu(II). In Frontier Orbital Theory, the highest occupied molecular orbital energy (E_{HOMO}) and the lowest unoccupied molecular orbital energy (E_{LUMO}) are commonly utilized to relate the spectral properties of compounds; moreover, it is also essential to identify and understand the nature of various segments of the compounds. The levels of electron density observed in the different regions of our compound can be indexed to electrophilic and nucleophilic segments. Figure 12 shows the electron charge distributions of the HOMO as electron donors and LUMO as electron acceptors. The HOMO and LUMO energies of Fe_3O_4/SiO_2/APTS

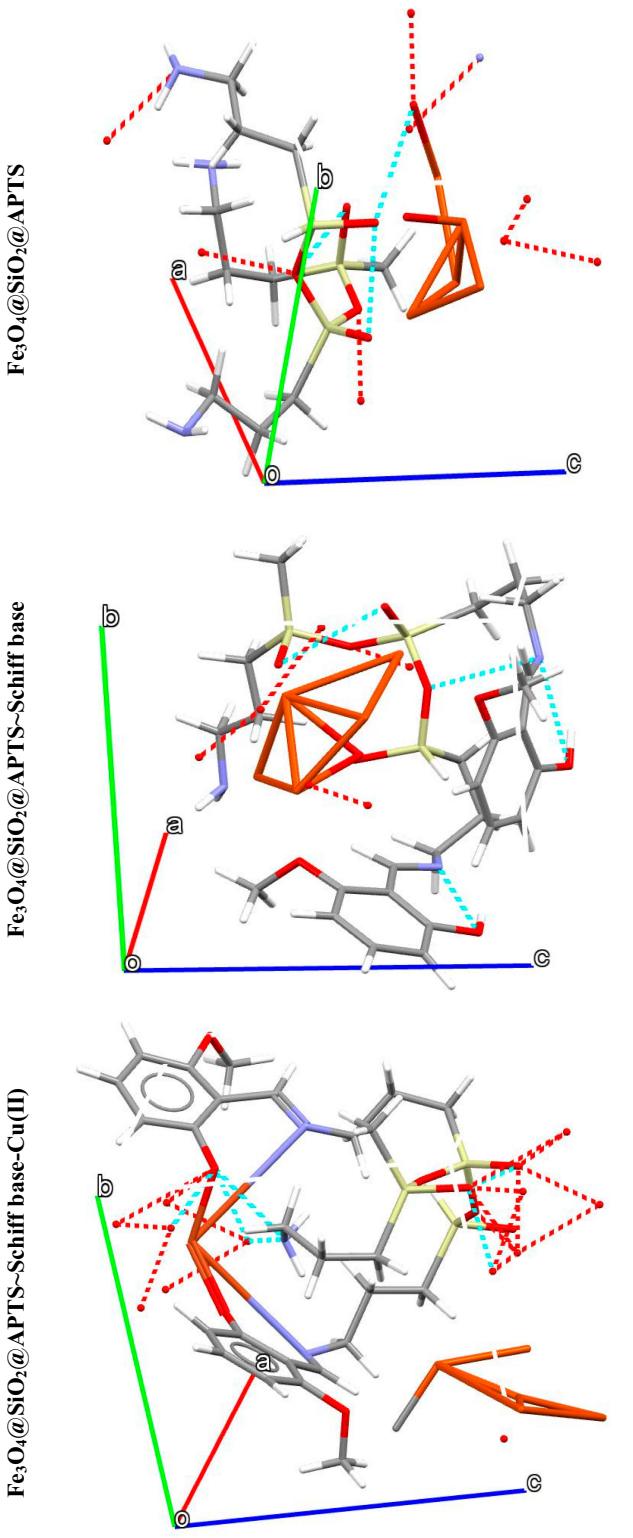

Figure 11 Intermolecular and π–π stacking interactions in the structures of Fe_3O_4/SiO_2/APTS, Fe_3O_4/SiO_2/APTS~Schiff base and Fe_3O_4/SiO_2/APTS~Schiff base-Cu (II). a, b and c: Structural orientations of compound formation.

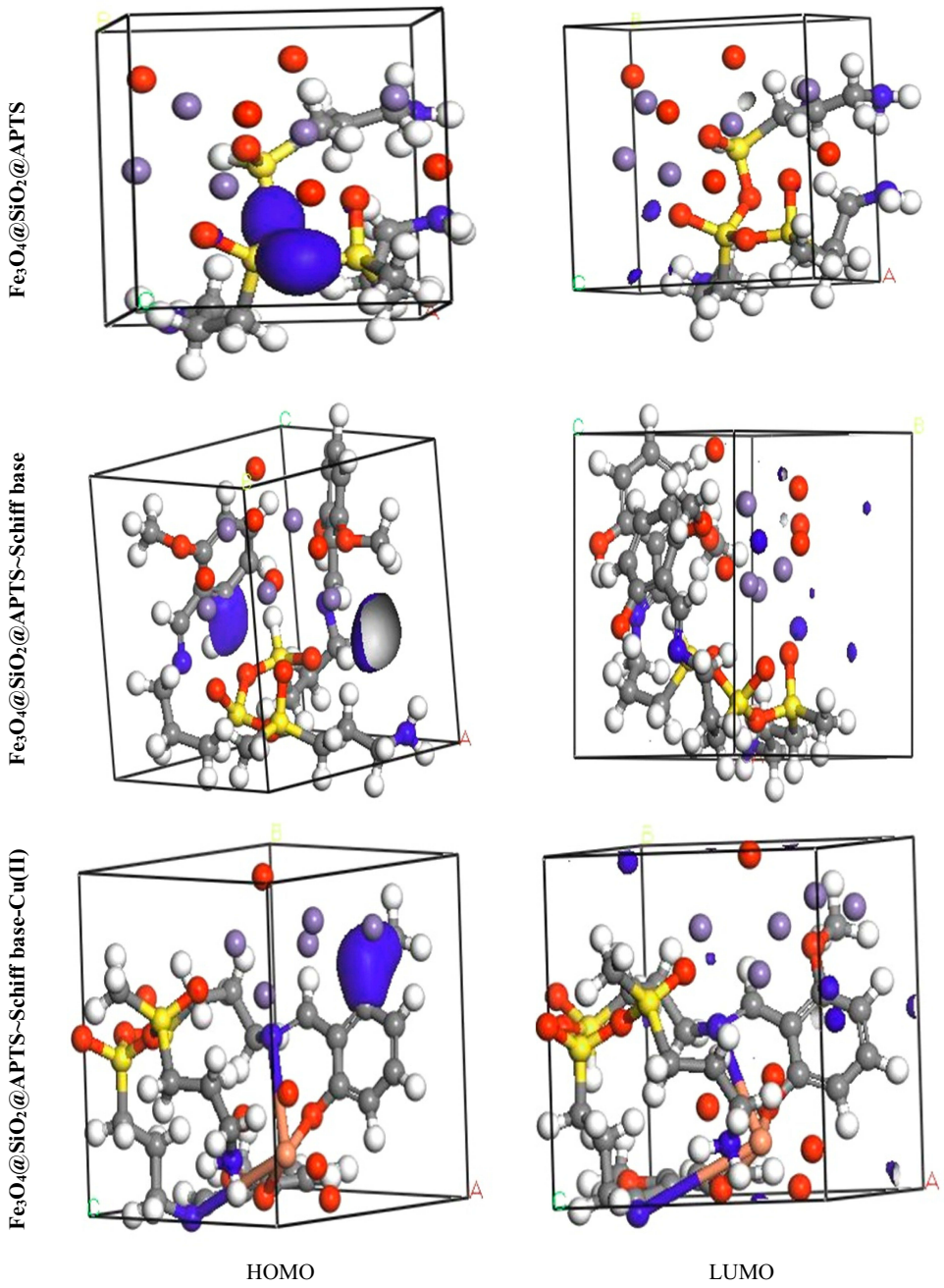

Figure 12 Frontier orbital density distributions (HOMO and LUMO) for Fe_3O_4, Fe_3O_4/SiO_2/APTS, Fe_3O_4/SiO_2/APTS~Schiff base and Fe_3O_4/SiO_2/APTS~Schiff base-Cu(II) in aqueous phase.

compounds were −19.83 and +5.808 eV, respectively. The HOMOs are principally localized on silica while the LUMOs are localized approximately on metal center. Furthermore, the HOMO and LUMO energies of Fe_3O_4/SiO_2/APTS~Schiff base were −23.245 and +5.779 eV, respectively. The HOMOs are largely localized on the OH of benzene ring and C of benzene ring while the LUMOs are generally localized on the O of core fragment. Also, the HOMOs and LUMOs of Fe_3O_4/SiO_2/APTS~Schiff base-Cu(II) at −22.878 and +5.265 eV, respectively, can be assigned to the aromatic rings. The conventional HOMO–LUMO gap, $\Delta E=E_{LUMO} - E_{HOMO}$ of Fe_3O_4/SiO_2/APTS, Fe_3O_4/SiO_2/APTS~Schiff base, and Fe_3O_4/SiO_2/APTS~Schiff base-Cu(II) was 25. 63, 29.02, and 28.143 eV. Furthermore, based on our analysis, molecular dynamic simulations, having

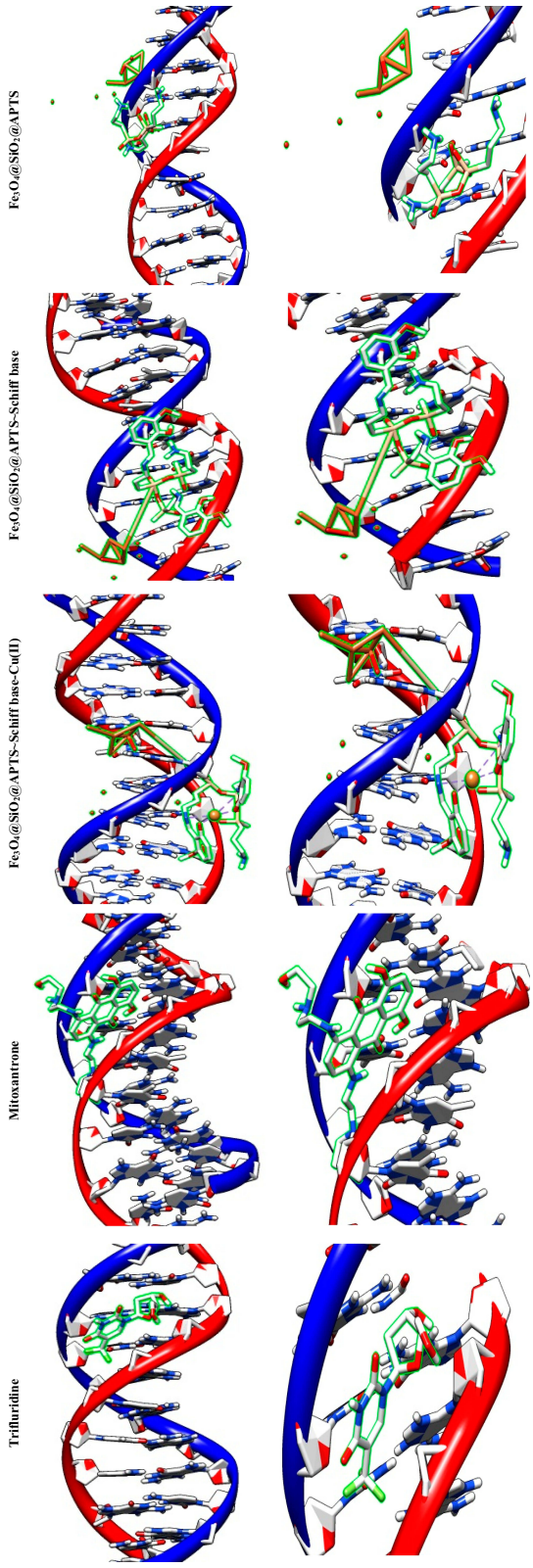

Figure 13 Docking conformation of Fe_3O_4/SiO_2/APTS; Fe_3O_4/SiO_2/APTS~Schiff base; Fe_3O_4/SiO_2/APTS~Schiff base-Cu(II) and Doxorubicin with Topoisomerase II (4fm9).

four-coordinated metal centers with two nitrogen and two oxygen atoms from Schiff bases, included a distorted tetrahedral coordination sphere.

Molecular Docking Compounds with BNA

Some anticancer drugs prohibit cell division through interaction with DNA or inhibition of topoisomerases; however, they also have severe side effects. Over the recent years, development of metal-based drugs as antitumor drugs and the binding capability of DNA or protein by noncovalent modes with no or fewer side effects have been regarded as an active field of research.[51] The reason behind such scientific interest is that these reagents are capable of interacting with DNA to cause mutations-physical of DNA and inhibit the growth of the tumor cells. Therefore, there has been much scientific research on the compounds that interact with DNA through non-covalent interaction (the major (G–C) or minor (A–T) grooves of nucleic acid) and reversibly via electrostatic, and intercalation. Docking technique is the most optimal approach to understand drug–DNA interactions, the proper orientation, and molecular mechanism and to elucidate binding mode/modes of a compound with DNA through non-covalent interactions, including major and minor groove binding.[52] Conformation of docked compounds and anticancer drugs and DNA such as Mitoxantrone and Trifluridine was analyzed in terms of vdW + Hbond + desolv Energy (kcal/mol). The binding free energy values were dominated by the vdW + Hbond + desolv (kcal/mol) negative energy values, implying that the binding events of the compounds were spontaneous. Figure 13 and Table 2 show the docked conformation of the compounds with the lowest free energy ($\Delta G_{binding}$). The values of docking energy were −10.35, −5.56, −10.85, −7.60, and −10.89 kcal/mol for Mitoxantrone, Trifluridine, Fe_3O_4/SiO_2 /APTS, Fe_3O_4/SiO_2/APTS~Schiff base, and Fe_3O_4/SiO_2 /APTS~Schiff base-Cu(II) docked to DNA, respectively. Based on the calculated binding free energies ($\Delta G_{binding}$), affinity of Fe_3O_4/SiO_2/APTS, Fe_3O_4/SiO_2/APTS~Schiff base and Fe_3O_4/SiO_2/APTS~Schiff base-Cu(II) to DNA double helix was more significant than Trifluridine (as DNA-drug interaction). Fe_3O_4/SiO_2/APTS and Fe_3O_4 /SiO_2/APTS~Schiff base-Cu(II) preferably bound to DNA in the minor groove. However, Fe_3O_4/SiO_2 /APTS~Schiff base interacted with DNA through the

Table 2 DNA Docking Results of the Compounds[a] (Unit: kcal/Mol)

Structures	Estimated Free Energy of Binding* (kcal/mol)	Final Intermolecular Energy (kcal/mol)	vdW + Hbond + Desolv Energy (kcal/mol)	Electrostatic Energy (kcal/mol)	Final Total Internal Energy (kcal/mol)	Torsional Free Energy (kcal/mol)	Unbound System's Energy (kcal/mol)
Mitoxantrone	−10.35	−15.07	−11.84	−3.23	−4.48	+4.77	−4.48
Trifluridine	−5.56	−6.93	−6.85	−0.09	−0.82	+1.37	−0.82
Fe_3O_4/SiO_2 /APTS	−10.85	−11.20	−10.39	−5.67	−1.58	+5.21	−1.58
Fe_3O_4/SiO_2 /APTS~Schiff base	−7.60	−14.46	−13.29	−1.17	−4.56	+6.86	−4.56
Fe_3O_4/SiO_2 /APTS~Schiff base-Cu(II)	−10.89	−14.18	−12.38	−1.8	−2.59	+3.29	−2.59

Notes: [a]To predict the drug–DNA interactions. *$\Delta G_{binding} = \Delta G_{vdW+hb+desolv} + \Delta G_{elec} + \Delta G_{total} + \Delta G_{tor}\ \Delta G_{unb}$.

Table 3 DNA Docking Results of the Compounds Towards a/T and G/C (Unit: kcal/Mol)

Complex	A-T	G-C
Fe_3O_4/SiO_2/APTS	−12.92	−11.86
Fe_3O_4/SiO_2/APTS~Schiff base	−9.67	−8.06
Fe_3O_4/SiO_2/APTS~Schiff base-Cu(II)	−9.16	−7.92

major groove. Compounds significantly bound to the minor groove of DNA and were not easily accessible to the oxidants. The minor groove is particularly an interesting target for small molecules since the closeness of the strands allows for more intimate contact on the surface area, and firmly binds with best fitting. The binding free energies ($\Delta G_{binding}$) of Fe_3O_4/SiO_2/APTS, Fe_3O_4/SiO_2 /APTS~Schiff base, and Fe_3O_4/SiO_2/APTS~Schiff base-Cu(II) to A/T were −12.92, −9.67, and −8.27 kcal/mol, respectively. However, the relative binding energies of docked Fe_3O_4/SiO_2/APTS, Fe_3O_4/SiO_2/APTS~Schiff base, and Fe_3O_4/SiO_2/APTS~Schiff base-Cu(II) with DNA were estimated to be −11.86, −8.06, and −7.92 kcal/mol for G/C, respectively (Table 3). Therefore, in the present research, compounds were more selective compared with A/T sequences than G/C sequences in DNA.

Molecular Docking Compounds with Topoisomerase II (4fm9)

Topoisomerases are essential nuclear enzymes regulating DNA topology by breaking the sugar-phosphate backbone of the genetic material and passing a second double helix through the nucleic acid gate. Therefore, studies on the interaction between modified and synthetic compounds

Table 4 Topoisomerase II Docking Results of Compounds[a] (Unit: kcal/Mol)

Structures	Estimated Free Energy of Binding* (kcal/mol)	Final Intermolecular Energy (kcal/mol)	vdW + Hbond + Desolv Energy (kcal/mol)	Electrostatic Energy (kcal/mol)	Final Total Internal Energy (kcal/mol)	Torsional Free Energy (kcal/mol)	Unbound System's Energy (kcal/mol)
Doxorubicin	−6.94	−10.22	−8.37	+1.85	−4.88	+3.28	−4.88
Fe_3O_4/SiO_2 /APTS	−7.70	−14.03	−7.52	−6.51	−2.45	+6.26	−2.45
Fe_3O_4/SiO_2 /APTS~Schiff base	−7.25	−10.55	−8.50	−8.50	−4.16	+3.29	−4.16
Fe_3O_4/SiO_2 /APTS~Schiff base-Cu(II)	−7.68	−11.26	−8.74	−2.52	−4.39	+3.58	−4.39

Notes: [a]To predict the drug–Topoisomerase II interactions. *$\Delta G_{binding} = \Delta G_{vdW+hb+desolv} + \Delta G_{elec} + \Delta G_{total} + \Delta G_{tor}\ \Delta G_{unb}$.

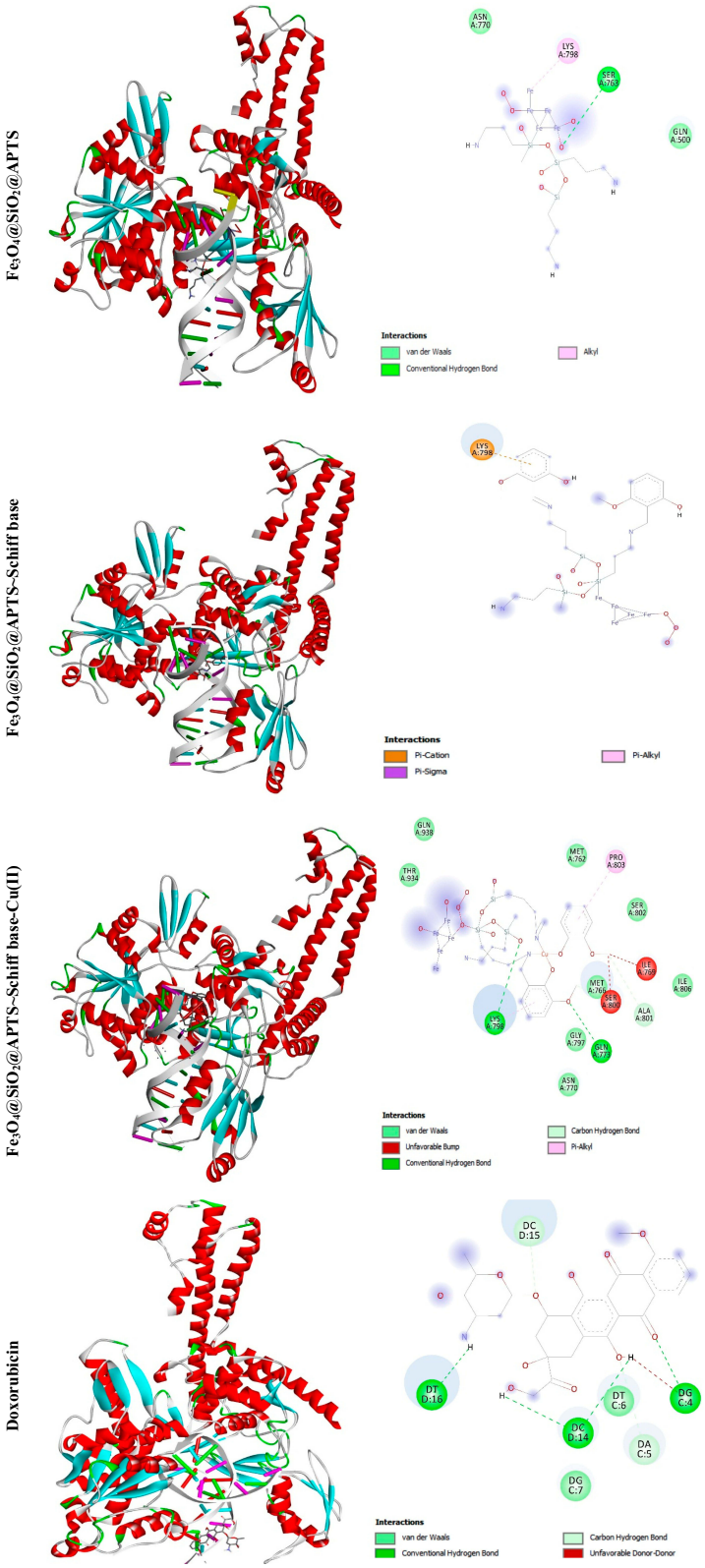

Figure 14 Docking conformation of Fe_3O_4@SiO_2@APTS; Fe_3O_4@SiO_2@APTS~Schiff base; Fe_3O_4@SiO_2@APTS~Schiff base-Cu(II) and Doxorubicin with Topoisomerase II (4fm9).

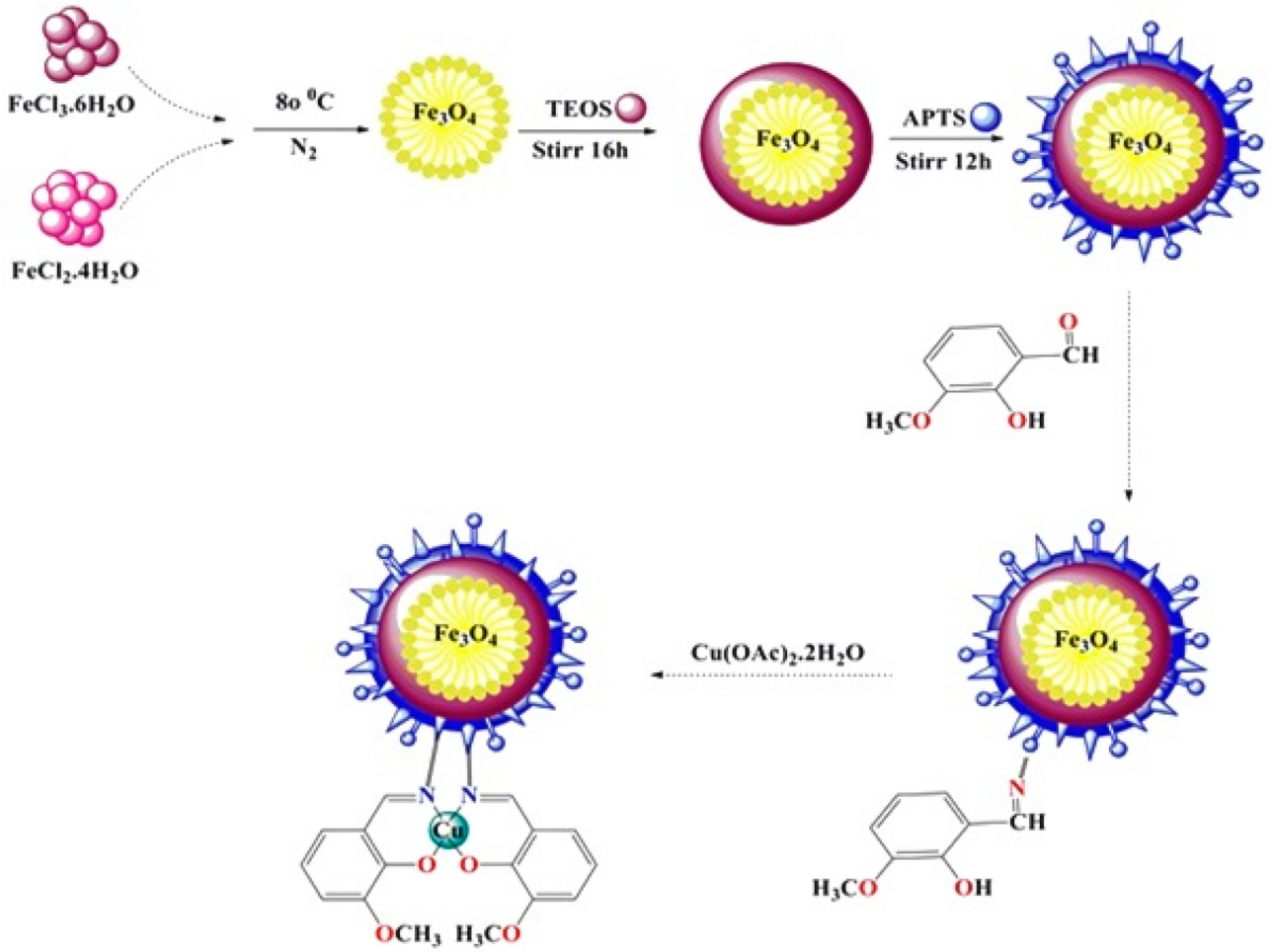

Scheme 1 The path used to synthesize magnetite NPs functionalized with the organo-silane molecules.

and DNA intercalators are very important because topoisomerase inhibitors play a major role in the treatment of cancer. The structure-based design of type II inhibitors (as very effective anticancer drugs with targets) by computational methods has been successfully applied in many drug design projects.[53,54] The resulting relative binding energy (the vdW + Hbond + desolv (kcal/mol) negative energy values) of docked Doxorubicin, Fe_3O_4/SiO_2/APTS, Fe_3O_4/SiO_2/APTS~Schiff base, and Fe_3O_4/SiO_2/APTS~Schiff base-Cu(II) with DNA binding site of topoisomerase II were observed to be −6.94, −7.70, −7.25, and −7.68 kcal/mol, respectively (Table 4). As shown in Figure 14, all compounds interacted with the DNA binding site of Topoisomerase II, thereby resulting in inhibitory effects on Topo II; moreover, the water of Fe_3O_4/SiO_2/APTS further formed mediated hydrogen bond with Ser A: 763, van der waals bond with Asn A:770, and Gln A:500 residues in close proximity to Lys A: 798 residues. However, Fe_3O_4/SiO_2/APTS~Schiff base did not strongly interact with Topo II and was stabilized by strong Pi-cation interaction with Lys A:798. Moreover, the interaction between Fe_3O_4/SiO_2/APTS~Schiff base-Cu(II) and receptor was dominated by hydrogen bond (Lys A:798 and Gln A:773), Pi-Alkyl (Pro A:803), and other bonds (Van der Waals, unfavorable bond, and carbon-hydrogen bond). The docked conformation into the DNA binding site of Topo-II revealed that Doxorubicin was situated in DT D:16, DC D:14, DG C:4, DC D:15, DG C:7, and DA C:5. The results of molecular docking showed that Fe_3O_4/SiO_2/APTS is a potential therapeutic strategy for developing novel chemotherapeutic drugs such as Topo-II inhibitors as concerns the treatment of cancers.

Conclusion

The core–shell of magnetite (Fe_3O_4/SiO_2) nanoparticles (MNPs) coated with (3-aminopropyl)triethoxysilane was

prepared and further linked with 2-hydroxy-5-nitrobenzaldehyde by the reaction between $–NH_2$ (linker) and –COH (aldehyde). Ultimately, Fe_3O_4/SiO_2/APTS(~NH_2)~Schiff base-Cu(II) nanoparticles were successfully synthesized. All nanoparticles were characterized by FT-IR, XRD, FE-SEM, TEM, and VSM analyses. FT-IR confirmed the successful immobilization of Schiff base group on the magnetic nanoparticles. In addition, the cytotoxic assay of nanoparticles was performed against K562 cell lines. The results revealed that Fe_3O_4/SiO_2/APTS(~NH_2) was the most cytotoxic in comparison with other nanoparticles of synthesized in the current research. The apoptosis-inducing activity was further assessed by AO/EB (Acridine Orange/Ethidium bromide) staining assay. The cytotoxic assay results of nanoparticles showed the interaction between the surface charge of the particles (positively charged NH_2 and negatively charged OH) and the cell wall. The compound structures were specified by quantum calculations. The energy (eV), space group, lattice parameters (Aº), unit cell parameters (Aº), and electron density of the predicted structures were obtained from the CASTEP module of Materials Studio. Furthermore, a docking study was conducted to ascertain the mode of action towards the molecular targets of DNA and topoisomerase II with compounds and anticancer drugs.

Acknowledgment

We thank Semnan University of Medical Sciences for supporting this study.

Disclosure

The authors report no conflicts of interest in this work.

References

1. Neuberger T, Schöpf B, Hofmann H, Hofmann M, Von Rechenberg B. Superparamagnetic nanoparticles for biomedical applications: possibilities and limitations of a new drug delivery system. *J Magn Magn Mater*. 2005;293(1):483–496. doi:10.1016/j.jmmm.2005.01.064
2. Feng B, Hong R, Wang L, et al. Synthesis of Fe3O4/APTES/PEG diacid functionalized magnetic nanoparticles for MR imaging. *Colloids Surf a Physicochem Eng Asp*. 2008;328(1–3):52–59. doi:10.1016/j.colsurfa.2008.06.024
3. Gupta AK, Curtis AS. Surface modified superparamagnetic nanoparticles for drug delivery: interaction studies with human fibroblasts in culture. *J Mater Sci*. 2004;15(4):493–496. doi:10.1023/b:jmsm.0000021126.32934.20
4. Onar K, Yakinci M, Synthesis of Fe3O4 nanoparticles for biomedical applications. Journal of Physics: Conference Series, IOP Publishing; 2016:012005.
5. Wu M, Huang S. Magnetic nanoparticles in cancer diagnosis, drug delivery and treatment. *Mol Clin Oncol*. 2017;7(5):738–746. doi:10.3892/mco.2017.1399
6. Mahdavi M, Ahmad M, Haron M, et al. Synthesis, surface modification and characterisation of biocompatible magnetic iron oxide nanoparticles for biomedical applications. *Molecules*. 2013;18(7):7533–7548. doi:10.3390/molecules18077533
7. Douziech-Eyrolles L, Marchais H, Herve K, et al. Nanovectors for anticancer agents based on superparamagnetic iron oxide nanoparticles, International. *J Nanomed*. 2007;2(4):541.
8. Xiao Y, Du J. Superparamagnetic nanoparticles for biomedical applications. *J. Mater Chem. B*. 2019;8:354-367.
9. Luo Y, Wang Q. Recent advances of chitosan and its derivatives for novel applications in food science. *J Food Process Beverages*. 2013;1(1):1–13.
10. Kesavan MP, Kotla NG, Ayyanaar S, et al. A theranostic nanocomposite system based on iron oxide-drug nanocages for targeted magnetic field responsive chemotherapy. *Nanomedicine*. 2018;14(5):1643–1654. doi:10.1016/j.nano.2018.04.013
11. Kesavan MP, Ayyanaar S, Lenin N, Sankarganesh M, Dhaveethu Raja J, Rajesh J. One pot synthesis of new poly (vinyl alcohol) blended natural polymer based magnetic hydrogel beads: controlled natural anticancer alkaloid delivery system. *J Biomed Mater Res A*. 2018;106(2):543–551. doi:10.1002/jbm.a.36262
12. Choi K-H, Nam K, Cho G, Jung J-S, Park B. Enhanced photodynamic anticancer activities of multifunctional magnetic nanoparticles (Fe3O4) Conjugated with Chlorin e6 and folic acid in prostate and breast cancer cells. *Nanomaterials*. 2018;8(9):722. doi:10.3390/nano8090722
13. Ranmadugala D, Ebrahiminezhad A, Manley-Harris M, Ghasemi Y, Berenjian A. Impact of 3–aminopropyltriethoxysilane-coated iron oxide nanoparticles on menaquinone-7 production using B. subtilis. *Nanomaterials*. 2017;7(11):350. doi:10.3390/nano7110350
14. Akbarzadeh A, Mikaeili H, Zarghami N, Mohammad R, Barkhordari A, Davaran S. Preparation and *in vitro* evaluation of doxorubicin-loaded Fe3O4 magnetic nanoparticles modified with biocompatible copolymers. *Int J Nanomedicine*. 2012;7:511. doi:10.2147/IJN.S30631
15. Liu X, Yin G, Yi Z, Duan T. Silk fiber as the support and reductant for the facile synthesis of Ag–Fe3O4 nanocomposites and its antibacterial properties. *Materials*. 2016;9(7):501. doi:10.3390/ma9070501
16. Chang M, Lin W-S, Xiao W, Chen Y-N. Antibacterial effects of magnetically-controlled Ag/Fe3O4 nanoparticles. *Materials*. 2018;11(5):659. doi:10.3390/ma11050659
17. Azadbakht B, Afarideh H, Ghannadi-Maragheh M, Bahrami-Samani A, Asgari M. Preparation and evaluation of APTES-PEG coated iron oxide nanoparticles conjugated to rhenium-188 labeled rituximab. *Nucl Med Biol*. 2017;48:26–30. doi:10.1016/j.nucmedbio.2016.05.002
18. Nigam S, Bahadur D. Dendrimerized magnetic nanoparticles as carriers for the anticancer compound, epigallocatechin gallate. *IEEE Trans Magn*. 2016;52(6):1–5. doi:10.1109/TMAG.2016.2517602
19. Saif B, Wang C, Chuan D, Shuang S. Synthesis and characterization of Fe3O4 coated on APTES as carriers for morin-anticancer drug. *J Biomater Nanobiotechnol*. 2015;6(04):267. doi:10.4236/jbnb.2015.64025
20. Niemirowicz K, Prokop I, Wilczewska AZ, et al. Magnetic nanoparticles enhance the anticancer activity of cathelicidin LL-37 peptide against colon cancer cells. *Int J Nanomedicine*. 2015;10:3843. doi:10.2147/IJN.S76104
21. Kesavan MP, Ayyanaar S, Vijayakumar V, et al. Magnetic iron oxide nanoparticles (MION s) cross-linked natural polymer-based hybrid gel beads: controlled nano anti-TB drug delivery application. *J Biomed Mater Res A*. 2018;106(4):1039–1050. doi:10.1002/jbm.a.36306

22. Ayyanaar S, Kesavan MP, Sivaraman G, et al. A novel curcumin-loaded PLGA micromagnetic composite system for controlled and pH-responsive drug delivery. *Colloids Surf A Physicochem Eng Asp*. 2019;573:188–195. doi:10.1016/j.colsurfa.2019.04.062
23. Tapiero H, Townsend D, Tew K. Trace elements in human physiology and pathology. copper. *Biomed Pharmacother*. 2003;57(9):386–398. doi:10.1016/S0753-3322(03)00012-X
24. Wang C, Liu L, Zhang L, Peng Y, Zhou F. Redox reactions of the α-synuclein− Cu2+ complex and their effects on neuronal cell viability. *Biochemistry*. 2010;49(37):8134–8142. doi:10.1021/bi1010909
25. El-Youssef M. Wilson disease. Mayo Clinic Proceedings, Elsevier; 2003: 1126–1136.
26. Dexter D, Wells F, Lee A, et al. Increased nigral iron content and alterations in other metal ions occurring in brain in Parkinson's disease. *J Neurochem*. 1989;52(6):1830–1836. doi:10.1111/j.1471-4159.1989.tb07264.x
27. Fahimirad B, Rajabi M, Elhampour A. A rapid and simple extraction of anti-depressant drugs by effervescent salt-assisted dispersive magnetic micro solid-phase extraction method using new adsorbent Fe3O4@ SiO2@ N3. *Anal Chim Acta*. 2019;1047:275–284. doi:10.1016/j.aca.2018.10.028
28. Ma M, Zhang Y, Yu W, Shen H-Y, Zhang H-Q, Gu N. Preparation and characterization of magnetite nanoparticles coated by amino silane. *Colloids Surf A Physicochem Eng Asp*. 2003;212(2–3):219–226. doi:10.1016/S0927-7757(02)00305-9
29. Heiney PA, Grüneberg K, Fang J, Dulcey C, Shashidhar R. Structure and growth of chromophore-functionalized (3-aminopropyl) triethoxysilane self-assembled on silicon. *Langmuir*. 2000;16(6):2651–2657. doi:10.1021/la990557w
30. Ramesh S, Felner I, Koltypin Y, Gedanken A. Reaction pathways at the iron–microspherical silica interface: mechanistic aspects of the formation of target iron oxide phases. *J Mater Res*. 2000;15(4):944–950. doi:10.1557/JMR.2000.0135
31. Yamaura M, Camilo R, Sampaio L, Macedo M, Nakamura M, Toma H. Preparation and characterization of (3-aminopropyl) triethoxysilane-coated magnetite nanoparticles. *J Magn Magn Mater*. 2004;279(2–3):210–217. doi:10.1016/j.jmmm.2004.01.094
32. Esmaeilpour M, Sardarian AR, Javidi J. Schiff base complex of metal ions supported on superparamagnetic Fe3O4@ SiO2 nanoparticles: an efficient, selective and recyclable catalyst for synthesis of 1, 1-diacetates from aldehydes under solvent-free conditions. *Appl Catal A Gen*. 2012;445:359–367. doi:10.1016/j.apcata.2012.09.010
33. Ghorbani-Choghamarani A, Ghasemi B, Safari Z, Azadi G. Schiff base complex coated Fe3O4 nanoparticles: a highly reusable nanocatalyst for the selective oxidation of sulfides and oxidative coupling of thiols. *Catal Commun*. 2015;60:70–75. doi:10.1016/j.catcom.2014.11.007
34. Shagholani H, Ghoreishi SM, Mousazadeh M. Improvement of interaction between PVA and chitosan via magnetite nanoparticles for drug delivery application. *Int J Biol Macromol*. 2015;78:130–136. doi:10.1016/j.ijbiomac.2015.02.042
35. Lee JH, Ju JE, Kim BI, et al. Rod-shaped iron oxide nanoparticles are more toxic than sphere-shaped nanoparticles to murine macrophage cells. *Environ Toxicol Chem*. 2014;33(12):2759–2766. doi:10.1002/etc.2735
36. Patil U, Adireddy S, Jaiswal A, Mandava S, Lee B, Chrisey D. *In vitro*/*in vivo* toxicity evaluation and quantification of iron oxide nanoparticles. *Int J Mol Sci*. 2015;16(10):24417–24450. doi:10.3390/ijms161024417
37. Lunov O, Syrovets T, Röcker C, et al. Lysosomal degradation of the carboxydextran shell of coated superparamagnetic iron oxide nanoparticles and the fate of professional phagocytes. *Biomaterials*. 2010;31(34):9015–9022. doi:10.1016/j.biomaterials.2010.08.003
38. Laskar A, Ghosh M, Khattak SI, Li W, Yuan X-M. Degradation of superparamagnetic iron oxide nanoparticle-induced ferritin by lysosomal cathepsins and related immune response. *Nanomedicine*. 2012;7(5):705–717. doi:10.2217/nnm.11.148
39. Lévy M, Lagarde F, Maraloiu V-A, et al. Degradability of superparamagnetic nanoparticles in a model of intracellular environment: follow-up of magnetic, structural and chemical properties. *Nanotechnology*. 2010;21(39):395103. doi:10.1088/0957-4484/21/39/395103
40. Valko M, Leibfritz D, Moncol J, Cronin MT, Mazur M, Telser J. Free radicals and antioxidants in normal physiological functions and human disease. *Int J Biochem Cell Biol*. 2007;39(1):44–84. doi:10.1016/j.biocel.2006.07.001
41. Bhasin G, Kauser H, Athar M. Iron augments stage-I and stage-II tumor promotion in murine skin. *Cancer Lett*. 2002;183(2):113–122. doi:10.1016/S0304-3835(02)00116-7
42. Voinov MA, Pagán JOS, Morrison E, Smirnova TI, Smirnov AI. Surface-mediated production of hydroxyl radicals as a mechanism of iron oxide nanoparticle biotoxicity. *J Am Chem Soc*. 2010;133(1):35–41. doi:10.1021/ja104683w
43. Chang YK, Liu YP, Ho JH, Hsu SC, Lee OK. Amine-surface-modified superparamagnetic iron oxide nanoparticles interfere with differentiation of human mesenchymal stem cells. *J Orthop Res*. 2012;30(9):1499–1506. doi:10.1002/jor.22088
44. Shen M, Cai H, Wang X, et al. Facile one-pot preparation, surface functionalization, and toxicity assay of APTS-coated iron oxide nanoparticles. *Nanotechnology*. 2012;23(10):105601. doi:10.1088/0957-4484/23/10/105601
45. Alexiou C, Arnold W, Hulin P, et al. Magnetic mitoxantrone nanoparticle detection by histology, X-ray and MRI after magnetic tumor targeting. *J Magn Magn Mater*. 2001;225(1–2):187–193. doi:10.1016/S0304-8853(00)01256-7
46. Yang L, Kuang H, Zhang W, et al. Size dependent biodistribution and toxicokinetics of iron oxide magnetic nanoparticles in mice. *Nanoscale*. 2015;7(2):625–636. doi:10.1039/C4NR05061D
47. Nagaraj K, Velmurugan G, Sakthinathan S, Venuvanalingam P, Arunachalam S. Influence of self-assembly on intercalative DNA binding interaction of double-chain surfactant Co (iii) complexes containing imidazo [4, 5-f][1, 10] phenanthroline and dipyrido [3, 2-d: 2′-3′-f] quinoxaline ligands: experimental and theoretical study. *Dalton Trans*. 2014;43(48):18074–18086. doi:10.1039/C4DT02134G
48. Galluzzi L, Kroemer G. Necroptosis: a specialized pathway of programmed necrosis. *Cell*. 2008;135(7):1161–1163. doi:10.1016/j.cell.2008.12.004
49. Chen Q, Kang J, Fu C. The independence of and associations among apoptosis, autophagy, and necrosis. *Signal Transduct Target Ther*. 2018;3(1):1–11. doi:10.1038/s41392-018-0018-5
50. You L, Liu X, Fang Z, Xu Q, Zhang Q. Synthesis of multifunctional Fe3O4@ PLGA-PEG nano-niosomes as a targeting carrier for treatment of cervical cancer. *Mater Sci Eng C*. 2019;94:291–302. doi:10.1016/j.msec.2018.09.044
51. Malekshah RE, Salehi M, Kubicki M, Khaleghian A. Crystal structure, molecular docking, and biological activity of the zinc complexes with 2-thenoyltrifluoroacetone and N-donor heterocyclic ligands. *J Mol Struct*. 2017;1150:155. doi:10.1016/j.molstruc.2017.08.079
52. Shamsi M, Yadav S, Arjmand F. Synthesis and characterization of new transition metal {Cu (II), Ni (II) and Co (II)} l-phenylalanine–DACH conjugate complexes: *in vitro* DNA binding, cleavage and molecular docking studies. *J Photochem Photobiol B*. 2014;136:1–11. doi:10.1016/j.jphotobiol.2014.04.009
53. Malekshah RE, Salehi M, Kubicki M, Khaleghian A. Biological studies and computational modeling of two new copper complexes derived from *β*- diketones and their nano-complexes. *J Coord Chem*. 2019;72:1697–1714.
54. Hasinoff BB, Wu X, Nitiss JL, Kanagasabai R, Yalowich JC. The anticancer multi-kinase inhibitor dovitinib also targets topoisomerase I and topoisomerase II. *Biochem Pharmacol*. 2012;84(12):1617–1626. doi:10.1016/j.bcp.2012.09.023